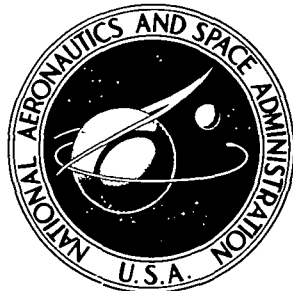


NASA CONTRACTOR
REPORT



N73-32287
NASA CR-2318

NASA CR-2318

CASE FILE COPY

MARTIAN THERMAL BOUNDARY LAYERS:
SUBHOURLY VARIATIONS INDUCED BY
RADIATIVE-CONDUCTIVE HEAT TRANSFER
WITHIN THE DUST-LADEN
ATMOSPHERE-GROUND SYSTEM

by A. J. Pallmann, W. P. Dannevik, and S. P. Frisella

Prepared by
SAINT LOUIS UNIVERSITY
Saint Louis, Mo. 63103
for Langley Research Center

NATIONAL AERONAUTICS AND SPACE ADMINISTRATION • WASHINGTON, D. C. • OCTOBER 1973

1. Report No. NASA CR-2318	2. Government Accession No.	3. Recipient's Catalog No.	
4. Title and Subtitle MARTIAN THERMAL BOUNDARY LAYERS: SUBHOURLY VARIATIONS INDUCED BY RADIATIVE-CONDUCTIVE HEAT TRANSFER WITHIN THE DUST-LADEN ATMOSPHERE-GROUND SYSTEM		5. Report Date October 1973	
7. Author(s) A. J. Pallmann, W. P. Dannevik, and S. P. Frisella		6. Performing Organization Code	
9. Performing Organization Name and Address SAINT LOUIS UNIVERSITY 221 N. GRAND SAINT LOUIS, MISSOURI 63103		8. Performing Organization Report No. PLATMOS RES REPT No. 8	
12. Sponsoring Agency Name and Address NATIONAL AERONAUTICS AND SPACE ADMINISTRATION WASHINGTON, DC 20546		10. Work Unit No. 185-47-91-0200	
15. Supplementary Notes This is a final report.		11. Contract or Grant No. NGL 26-006-016	
16. Abstract Radiative-conductive heat transfer has been investigated for the ground-atmosphere system of the planet Mars. The basic goal was the quantitative determination of time-dependent vertical distributions of temperature and static stability for southern-hemispheric summer season and middle and polar latitudes, for both dust-free and dust-laden atmospheric conditions.			
The numerical algorithm, which models at high spatial and temporal resolution the thermal energy transports in the dual ground-atmosphere system, is based on solution of the applicable heating-rate equation, including radiative and molecular-conductive heat transport terms. The two subsystems are coupled by an internal thermal boundary condition applied at the ground-atmosphere interface level. Initial data and input parameters are based on Mariner 4, 6, 7, and 9 measurements and the JPL Mars Scientific Model. Numerical experiments were run for dust-free and dust-laden conditions in the midlatitudes, as well as ice-free and ice-covered polar regions. Representative results and their interpretation are presented.			
Finally, the theoretical framework of the generalized problem with non-conservative Mie scattering and explicit thermal-convective heat transfer is formulated, and applicable solution algorithms are outlined.			
17. Key Words (Suggested by Author(s)) Martian Atmosphere Thermal Boundary Layer Dust-laden Atmosphere Radiative Heat Transfer Conductive Heat Transfer Ground-Atmosphere Interface Energetics	18. Distribution Statement Unclassified - unlimited		
19. Security Classif. (of this report) Unclassified	20. Security Classif. (of this page) Unclassified	21. No. of Pages 93	22. Price* Domestic, \$3.75 Foreign, \$6.25

FOREWORD

This is the final report of a several-years research project entitled "The Structure and Circulation of the Lower Martian Atmosphere," sponsored by the Planetary Atmospheres Section, NASA Langley Research Center, under Grant No. NGL-26-006-016.

In the exploratory stages of the project, it became apparent that a thorough investigation of the radiative-conductive transfer of thermal energy in the soil and atmospheric subsystems leads to a deeper understanding of the temperature field and static stability in an atmosphere which has a radiative responsiveness much greater than that on Earth. The research reported herein reflects this basic orientation.

Data from various Mariner spacecraft were readily made available by the Technical Information and Documentation Division of the Jet Propulsion Laboratory, Pasadena, California. Dr. W. A. Baum, Director of the Planetary Research Center at Lowell Observatory, Flagstaff, Arizona was most helpful in providing photographic information on the planet Mars. Finally, the authors wish to express their gratitude to Drs. R. A. Hanel and J. C. Pearl of the Goddard Space Flight Center for generously releasing Mariner 9 preliminary data.

TABLE OF CONTENTS

	Page
Foreword	iii
List of Figures	vii
Glossary of Symbols	ix
1.0 Introduction; Objectives of Report	1
2.0 A Physical-Mathematical Model of Martian Ground-Atmosphere Thermal Boundary Layers	4
2.1 Basic Physical Mechanisms	4
2.2 Development of the Mathematical Model	8
2.21 Physical Setting	8
2.22 Governing Relations	9
2.23 Boundary and Initial Conditions	11
2.24 Formulation of Mathematical Problem and Analytical Simplifications	13
3.0 Design of the Numerical Algorithm	18
3.1 Integration over Frequency and Computational Form of Transmission Function	18
3.2 Finite Difference Form of the Governing System of Equations	21
3.3 Input Data and Computational Procedure	26

	Page
4.0 Basic Numerical Experiments and Interpretation of Results	29
4.1 Description of Experiments	29
4.2 Results and Interpretation	30
4.21 Mariner 7 Midlatitudinal Experiment	30
4.22 Mariner 9 Midlatitudinal Experiment	33
4.23 Mariner 9 South-Polar Region Experiment	44
5.0 Theoretical Framework of the Generalized Problem	54
5.1 Background and Orientation	54
5.2 Basic Definitions and Fundamental Relations of Radiative Transfer	56
5.3 Solution of the Local Radiative Transfer Equation	59
5.4 Solution of the Thermal Energetics Problem	64
5.5 Modeling of the Time-Dependent Thermal Convection Layer Induced by Radiative Surface Heating	69
6.0 Summary of Research and Major Findings	73
References	79

LIST OF FIGURES

<u>Fig.</u>		<u>Page</u>
1. Temperature profiles in the lowest 400 m for various hours, Mar 7 Midlat. Experiment		31
2. Time-variation of molecular- conductive heating rate at the 12.5 m level		32
3. Diurnal tautochrone patterns near the interface layers		33
4. Vertical temperature profiles at 0500 and 1600 LMT, Mar 9 Midlat. Experiment		35
5. Diurnal tautochrone patterns, dust-free conditions		38
6. Diurnal history of component heat fluxes at ground-atmosphere interface		40
7. Height-time cross-sections of the temperature field for dust-free and dust-laden conditions		43
8. Schematic physical setting for the south polar ice cap region		44
9. Temperature profiles for dust-free and dust-laden conditions, from Day 1 of Mar 9 South-Polar Region Experiments		46
10. Diurnal history of planetary and solar radiative fluxes at the top of the dust layer		47
11. Temperature profiles for dust-laden conditions, from Day 2		48
12. Temperature profiles for dust-laden conditions, from Day 3		49
13. Temperature profiles for dust-laden conditions and a frost-free sand surface at latitude 80°S		51

GLOSSARY OF SYMBOLS

- b : radiative diffusivity factor
- c : specific heat
- d : mean spectral line spacing
- B_ν : Planck function
- B_ν : Planck Function matrix
- E_n : exponential integral of order n
- F_ν : total spectral net radiative flux
- F : matrix of Stokes parameters of the downwardly-directed radiative intensity at the top of the atmosphere
- G_ν : upwardly-directed hemispheric radiative flux at the interface level
- I_0, I_1 : Bessel function of the first kind of order 0 and 1, respectively, of imaginary argument
- \bar{I}_ν : matrix of Stokes parameters of the diffuse radiation field
- J_p : p-th Stokes parameter of the radiative source function
- k : thermal conductivity
- P : normalized scattering matrix
- p : atmospheric pressure
- S : integrated line intensity under standard thermodynamic conditions
- s : slant path length
- S_ν : spectral solar irradiance at the top of the atmosphere

t : time

T : temperature

x : depth, measured from top of the atmosphere

z : altitude

α_0 : mean half-width at STP

α_s : surface albedo

Γ : coefficient of temperature dependence of integrated line intensity

ϵ : surface IR emissivity

θ : zenith angle

K_v : mass absorption coefficient

μ : cosine of zenith angle

ξ : depth, measured from top of atmosphere

ρ : mass density

σ : Stefan-Boltzmann constant

Υ : transmission function

τ_v : optical depth

ϕ : azimuth angle

ω : albedo for single scattering

Subscripts

($_d$) : lowest depth considered in subsurface region

($_i$) : spectral quantity evaluated at i -th frequency interval

$(\cdot)_n$: discrete vertical coordinate level of ground-atmosphere interface

$(\cdot)_m$: discrete vertical coordinate level

$(\cdot)_p, (\cdot)_q$: p-th or q-th Stokes parameter

$(\cdot)_s$: ground-atmosphere interface level

Superscripts

$(\cdot)^a$: absorption

$(\cdot)^d$: dust-laden

$(\cdot)^{(n)}$: discrete time step (Section 3) or optical depth index (Section 5)

$(\cdot)^s$: scattering

1.0 Introduction; Objectives of Report

Among those characteristics of the Martian atmosphere which have important bearing on the nature of predominant atmospheric processes, one of the most essential is the capability of the atmosphere to respond rapidly and intensely to imbalances in the atmospheric radiation field. Because of this capability, it is likely that the Martian atmospheric circulation has a significant component which is directly driven by thermal gradients produced by differential radiative heating, with the resulting motion field having little impact on the redistribution of the thermal field itself (Gierasch and Goody, 1968).

Evidence for conditions conducive to a large radiative response capability on Mars has a firm basis in the data returned by the Mariner 4, 6, 7, and 9 spacecraft series. The Mariner 4 occultation experiments provided first indications that surface pressure was characteristically less than 10 mb, while spectroscopic measurements, particularly those performed by Mariner 6 and 7, confirmed a high concentration of CO₂ as major atmospheric constituent. Inversion of infrared interferometer spectrometer (IRIS) measurements (Mariner 9) have provided representative temperature soundings, although much work

remains to be done before the impact of suspended dust aerosol on IRIS-derived temperature distributions can be assessed.

In view of the importance of radiative processes in providing the elementary drive for Martian atmospheric circulation of various space scales, it is essential that we understand in detail the radiative exchange mechanisms, particularly those in the near-surface atmospheric layers. In the planetary boundary layer, and much more so in the surface boundary layer, a significant diurnal variation in thermal structure is induced in response to large surface temperature variations. It is in these layers that a large fraction of the conversion of insolation into atmospheric internal, potential, and kinetic energy takes place.

The direction taken by the research reported here has been influenced greatly by the preceding considerations. The objectives of this report are to describe a research program and numerical model designed to investigate the role of radiative processes in controlling the subhourly history of the Martian atmospheric thermal structure, and the time-dependent interplay between physical processes responsible for surface heating and those determining the

response of the atmospheric boundary layer to that heating. This type of investigation can contribute to a better understanding of the dynamical structure of the Martian planetary and surface boundary layers, which is important for Martian lander vehicle design and mission planning, and to a more complete characterization of the driving mechanism for larger-scale circulation.

As discussed in Section 2, the data base provided by the Mariner spacecraft series is sufficient to allow inferences into the basic physical mechanisms of radiative-conductive heat transfer in the Martian atmosphere-ground system. These inferences provide the basis for the numerical simulation model, which is described in Section 2.2 and Section 3. Section 4 relates the basic numerical experiments which have been performed with the model, and interpretation of results is undertaken. The theoretical framework for an expanded version of the model is described in Section 5, and Section 6 summarizes major findings of the research program.

2.0 A Physical-Mathematical Model of Martian Ground-Atmosphere Thermal Boundary Layers

2.1 Basic Physical Mechanisms

Inferences relating to the basic physical processes at work in the Martian ground-atmosphere system may be made on the basis of the observational evidence outlined in the Introduction. These inferences can then be used as a guide in developing a numerical model of heat exchange in the thermal boundary layer.

Of crucial importance in this context is the evidence for a relatively low surface pressure (~ 6 mb) and high concentration of carbon dioxide as atmosphere constituent. This combination of the predominance of a radiatively-active constituent gas and a relatively tenuous atmosphere results in an intense radiative response capability, so that heat exchange in the troposphere is dominated by radiative transfer for thermal perturbations of characteristic scale greater than 100 m.

Goody and Belton (1967) have obtained the preceding result through calculation of the time for relaxation of thermal perturbations by radiation, molecular conduction and

turbulent convection in a dust-free carbon dioxide model atmosphere. It is estimated that the Martian atmosphere radiatively responds to surface temperature variation to a height of several km, particularly if the surface variation is large over diurnal time periods.

The intense radiative response capability has a profound impact on Martian atmospheric dynamics. Gierasch and Goody (1968) contend on the basis of scaling estimates and relaxation time calculations that to first order the nonlinear advective feedback of mean velocity on the temperature field may be neglected in the Martian atmosphere. Hence, it is likely that a model which neglects advective temperature changes due to the mean wind field can provide meaningful information on the time-variation of thermal structure in the lower atmosphere (Gierasch, 1971).

A second crucial body of information provided by the Mariner observations is the evidence for a global extent of sand-like Martian soil material and lack of oceanic areas. These features permit largely-unattenuated insolation to induce a large diurnal soil surface temperature variation, especially in the absence of suspended dust particulates. Both Earth-based and Mariner radiometric scans indicate a diurnal variation of brightness temperature

of 50-80K at midlatitudes. In view of its radiative responsiveness, we may expect that the Martian atmosphere will respond significantly to this surface temperature variation, in addition to its direct response to solar heating. The latter is especially important if there exists an appreciable amount of suspended dust particulates.

Details of the coupling between Martian soil and atmospheric temperature variation due to radiative exchange depend crucially on the structure of the CO_2 absorption bands. Since most of the 15μ band absorbs strongly, even under the reduced surface pressure conditions of Mars (~ 6 mb), a portion of the coupling will occur through the near-surface and interface layers, where radiative transfer will approximate a diffusion process. On the other hand, spectral "gappiness" and weak-line transmission, each enhanced by atmospheric tenuity, will permit some long-range exchange of energy from the planetary surface to several scale heights and towards space. Absorption of direct solar radiation in the 4.3μ band, and the presence of lines of intermediate intensity, further complicate the heat transfer by radiative exchange.

The preceding considerations point to the necessity of considering the thermal coupling between ground and atmosphere subsystems in any model of the diurnal variation of Martian thermal boundary layer structure. Molecular thermal conduction in the soil material can account for an appreciable fraction of the net heat flux balance at the soil-atmosphere interface (Pallmann and Dannevik, 1972; Sellers, 1965), and requires knowledge of the subsurface temperature profile for its determination. Hence, calculation of the temporal variation of boundary layer thermal structure requires a simultaneous forward time-integration of the subsurface temperature distribution.

2.2 Development of the Mathematical Model

2.21 Physical Setting

The atmospheric model is taken to be that of a pure carbon dioxide atmosphere of 50 km depth, in local thermodynamic equilibrium, and exhibiting plane-parallel stratification. (However, as discussed later, the impact of suspended dust particulates on gaseous absorption will be taken into account by the model). Doppler broadening of spectral lines is assumed negligible, as well as the effects of molecular scattering.

The lower solid surface is taken to be either a flat, uniform sand-like material, or solid carbon dioxide. The surface diffusely reflects solar radiation in accordance with a radiometric albedo, and emits as a grey body. In the case of solid carbon dioxide, the interface temperature is assumed fixed at the solid-vapor equilibrium sublimation point, and the subsurface temperature field is isothermal. For all other cases, the ground-atmosphere interface temperature, as well as the subsurface profile, is determined as a function of time by the model.

2.22 Governing Relations

For the preceding physical setting, the applicable heating-rate equation takes the following form:

$$\rho c \frac{\partial T}{\partial t}(x,t) = \frac{\partial}{\partial x} \left\{ k \frac{\partial T}{\partial x} - \int_0^{\infty} F_v(x,t) dv \right\}, \quad 0 < x < x_s, t > 0$$
$$\rho_s c_s \frac{\partial T_s}{\partial t}(x,t) = \frac{\partial}{\partial x} \left\{ k_s \frac{\partial T_s}{\partial x} \right\}, \quad x_s < x < x_d, t > 0 \quad (1)$$

In (1), x is the vertical coordinate, measured from the top of the model atmosphere ($x=0$), x_s is the ground-atmosphere interface level, and x_d is the lowest subsurface level under consideration. Other notation is defined in the Glossary of Symbols.

The preceding equation neglects the production of heat by viscous dissipation, the advection of temperature by a mean velocity field, and the contribution by the rate of working through shear stresses. These approximations are complementary to the assumption that the advective feedback of velocity on the temperature field is negligible. In addition, it is assumed that no phase changes occur in the regions away from the interface level.

The right-hand side of (1) represents the convergence of total heat flux at the level x and time t . The first term represents the contribution of molecular thermal

conduction, and the second the impact of radiative flux at all wavelengths. Formulation of the preceding quantity is the subject of an earlier report (Pallmann, 1968).

The spectral radiative net flux for the case of local thermodynamic equilibrium may be expressed as

$$F_\nu(x,t) = 2\pi \int_0^x S_\nu(0) \exp(\int_0^\mu \rho K_\nu ds' \bar{\mu}') \mu d\mu + 2\pi \int_0^1 G_\nu(x_s) \exp(-\int_x^{x_s} \rho K_\nu ds' \bar{\mu}') \mu d\mu \\ - 2\pi \int_0^x \int_0^y B_\nu(\xi, t) \exp(-\int_x^\xi \rho K_\nu ds' \bar{\mu}') \rho K_\nu d\mu d\xi \\ - 2\pi \int_0^{x_s} \int_x^{x_s} B_\nu(\xi, t) \exp(-\int_x^\xi \rho K_\nu ds' \bar{\mu}') \rho K_\nu d\mu d\xi \quad (2)$$

In this expression, $S_\nu(0)$ is the intensity of radiation incident at the top of the atmosphere, and $G_\nu(x_s)$ is the upwardly-directed radiation at the soil-atmosphere interface level. The planetary radiation field is assumed to be axially symmetric. It may be seen from (2) that the total spectral radiative flux is a functional of the atmospheric temperature distribution, through its dependence on the Planck function.

To complete the mathematical model, boundary and initial conditions are required for (1).

2.23 Boundary and Initial Conditions

At the interface between atmospheric and soil subsystems, a discontinuity in physico-optical properties occurs, so that (1) is not directly applicable at this level. We may, however, derive an internal boundary condition on the assumption that the total heat flux must remain continuous across the interface. This is equivalent to the requirement that there can be no net accumulation of thermal energy in a layer of vanishing thickness, since this would lead to an unbounded temperature change. Considering the fluxes of solar and planetary radiation and molecular-conductive heat flux in the soil and atmospheric layers adjacent to the interface, the requirement of continuity of heat flux at $x=x_s$ takes the form

$$k_s \frac{\partial T_s}{\partial x} - k \frac{\partial T}{\partial x} - \epsilon \sigma T_s^4 (x_s, 0, t) + 2\pi \int_0^{x_s} \int_0^{\infty} \int_0^{\infty} B_{\nu}(s, t) \exp(-\int_{x_s}^s \rho K_{\nu} ds' \bar{\mu}') \rho K_{\nu} dv d\mu ds \\ + 2\pi \int_{-1}^0 \int_0^{\infty} (1-\alpha_s) \mu S_{\nu}(0) \exp(\int_0^{x_s} \rho K_{\nu} ds' \bar{\mu}') dv d\mu = 0 \quad (3)$$

In this relation, the heat flux due to phase changes has been omitted and solar radiation incident at the surface is assumed diffusely reflected.

To (3) may be added the requirement that soil and atmospheric temperatures are equal at the interface level.

This constitutes an assumption that temperature is continuous across the interface, which is complementary to the requirement of local thermodynamic equilibrium for the atmospheric subsystem. Thus, we have

$$T_s(x_s+0,t) = T(x_s-0,t) \quad (4)$$

in addition to relation (3).

In the case that the lower surface is solid carbon dioxide, the requirements (3) and (4) may be simplified since the interface temperature may be assumed equal to the CO₂ solid-vapor equilibrium value. Hence

$$T_s(x_s+0,t) = T(x_s-0,t) = T_{sub} \quad (5)$$

where T_{sub} is the sublimation temperature for carbon dioxide at the surface pressure.

At the upper and lower bounds of the solution domain, the temperature is assumed fixed at a known value:

$$T(0,t) = T_o, T_s(x_d,t) = T_d \quad (6)$$

If the absorption coefficients, thermal conductivity, density distribution, and physical properties at the interface are assumed given, then a known initial temperature distribution is all that is required to integrate the

system (1), (3) and (4) or (5), and (6) forward in time. The complete system of equations is presented in the following subsection, followed by some analytical simplifications to increase its tractability.

2.24 Formulation of the Mathematical Problem and Analytical Simplifications

The relations presented in the preceding discussion may be combined to pose the following boundary-initial-value problem:

Governing equation:

$$\rho c \frac{\partial T}{\partial t} = \frac{\partial}{\partial x} \left\{ k \frac{\partial T}{\partial x} + 2\pi \int_0^\infty \left[- \int_{-1}^0 S_\nu(0) \exp \left(\int_0^x \rho K_\nu ds \bar{\mu} \right) \mu d\mu - \int_x^1 G_\nu(x_s) \exp \left(- \int_x^s \rho K_\nu ds \bar{\mu} \right) \mu d\mu \right. \right. \\ \left. \left. + 2\pi \int_{-1}^0 \int_0^\nu B_\nu(\xi, t) \exp \left(- \int_\xi^x \rho K_\nu ds \bar{\mu} \right) \rho K_\nu d\xi d\mu + 2\pi \int_0^x \int_0^\nu B_\nu(\xi, t) \exp \left(- \int_\xi^x \rho K_\nu ds \bar{\mu} \right) \rho K_\nu d\xi d\mu \right] d\nu \right\} \quad (7a)$$

$$\rho_s c_s \frac{\partial T_s}{\partial t} = \frac{\partial}{\partial x} \left\{ k_s \frac{\partial T_s}{\partial x} \right\}, \quad x_s < x < x_d, \quad t > 0 \quad (7b)$$

Boundary conditions:

At $x=x_s$:

$$k_s \frac{\partial T_s}{\partial x} - k \frac{\partial T}{\partial x} - \varepsilon \sigma T_s^4(x_s-0, t) + 2\pi \int_0^{x_s} \int_{-1}^0 \int_0^\nu B_\nu(\xi, t) \exp \left(- \int_{x_s}^\xi \rho K_\nu ds \bar{\mu} \right) \rho K_\nu d\nu d\mu ds \\ + 2\pi \int_{-1}^0 \int_0^\infty (1-\alpha_s) \mu S_\nu(0) \exp \left(\int_0^x \rho K_\nu ds \bar{\mu} \right) d\nu d\mu = 0, \quad t > 0, \quad (8)$$

or,

$$T_s(x_s+0, t) = T(x_s-0, t) = T_{sub.}, \quad t \geq 0$$

At $x=0$:

$$T(0,t) = T_0, \quad t \geq 0 \quad (9a)$$

At $x=x_d$:

$$T_s(x_d,t) = T_d, \quad t \geq 0 \quad (9b)$$

Initial conditions:

$$\begin{aligned} T_s(x,0) &= T_{s_i}(x), \quad x_s \leq x \leq x_d, \\ T(x,0) &= T_l(x), \quad 0 \leq x \leq x_s \end{aligned} \quad (10)$$

The system (7) through (10) is sufficient to determine a unique solution for the distribution of temperature throughout the region $x_s \leq x \leq x_d$, for any time $t > 0$.

Before adapting the system (7) through (10) for numerical analysis, some simplifications in the analytical formulation can be made without seriously affecting the solution.

First, we consider the possibility of performing implicitly the integration over the cosine of zenith angle indicated in eqs. (7) through (8). Consider, for example, the integral in (7) having the form

$$\int_0^1 G_\nu(x_s) \exp\left(-\int_0^{x_s} \rho K_\nu ds' \bar{\mu}'\right) \mu d\mu \quad (11)$$

This expression involves the exponential integral of order n , defined as (Sparrow and Cess, 1966)

$$E_n(\psi) \equiv \int_0^1 \mu^{n-2} \exp(-\psi \bar{\mu}') d\mu \quad (12)$$

To a sufficient degree of approximation, the integral of order 3 behaves as a simple negative exponential:

$$2E_3(\psi) \approx e^{-b\psi}, \quad b = 1.66 \quad (13)$$

This approximation has been discussed by Elsasser (1960), Goody (1964), and Kondrat'yev (1969). Using the formula

$$\frac{dE_n(\psi)}{d\psi} = -E_{n-1}(\psi), \quad n = 2, 3, \dots$$

the integrals involving E_n may be replaced by approximations similar to (13), and the explicit integration over zenith angle is eliminated. The expression (2) for spectral net flux then appears as

$$\begin{aligned}
F_\nu(x, t) = & 2\pi S_\nu(0) \mu \exp\left(-\int_0^x \rho K_\nu ds' \bar{\mu}'\right) + 2\pi b^{-1} G_\nu(x_s) \exp\left(-b \int_{x_s}^x \rho K_\nu ds'\right) \\
& - 2\pi b^{-1} \int_0^x B_\nu(\xi, t) \frac{\partial}{\partial \xi} \left[\exp\left(-b \int_x^\xi \rho K_\nu ds'\right) \right] d\xi \\
& - 2\pi b^{-1} \int_x^{x_s} B_\nu(\xi, t) \frac{\partial}{\partial \xi} \left[\exp\left(-b \int_x^\xi \rho K_\nu ds'\right) \right] d\xi
\end{aligned} \tag{14}$$

where μ now refers to the cosine of solar zenith angle at the time t .

Similarly, the internal boundary condition (8) may be rewritten as

$$\begin{aligned}
k_s \frac{\partial T_s}{\partial x} - k \frac{\partial T}{\partial x} - \epsilon \sigma T_s^4(x_s=0, t) + 2\pi \int_0^{x_s} \int_0^\infty B_\nu(s, t) \exp\left(-\int_{x_s}^s b \rho K_\nu ds'\right) dy ds \\
+ 2\pi \int_0^\infty (1 - \alpha_s) S_\nu(0) \exp\left(-\int_0^s \rho K_\nu ds' \bar{\mu}'\right) \mu du = 0
\end{aligned} \tag{15}$$

It will be convenient for the computational version of (15) to simplify the grey body emission term $\epsilon \sigma T_s^4$. This term may be expanded around a reference temperature T_{s_0} , which will later be identified with the surface temperature at the beginning of a timestep in the numerical integration. Thus, we may write

$$\epsilon \sigma T_s^4(x_s=0, t) \approx 4\epsilon \sigma T_{s_0}^3 \left[T_s(x_s=0, t) - \frac{3}{4} T_{s_0} \right] \tag{16}$$

Since, on a relative scale, the surface temperature change over a single timestep is small, the representation (16) is

sufficiently accurate. With the approximation (16),
the finite-difference form of (15) appears as a linear
algebraic equation for the temperature $T_5(x_5=0, t)$ at the
end of a timestep.

3.0 Design of the Numerical Algorithm

3.1 Integration over Frequency and Computational Form of the Transmission Function.

The integration over frequency for the radiative flux terms in (7) and (8) will be accomplished by dividing the CO₂ absorption spectrum into small increments, within which the Planck function and solar spectral intensity will be assumed constant. This procedure leads to the consideration of the CO₂ transmission function, defined by

$$T_i(s_1, s_2) \equiv \frac{1}{\Delta\nu_i} \int_{\nu_i - \frac{\Delta\nu_i}{2}}^{\nu_i + \frac{\Delta\nu_i}{2}} \exp\left(-\int_{s_1}^{s_2} \rho(s) K_\nu(s, \nu) ds\right) d\nu$$

where $\Delta\nu_i$ is the frequency interval of interest, and s_1 and s_2 are the endpoints of the geometric slant path. It should be noted that the mass absorption coefficient is a function of temperature and equivalent pressure along the path length, and the transmission function must take into account the variation of these gas-kinetic properties over the distance $|s_1 - s_2|$.

The intricate fine structure of the CO₂ vibration-rotation bands make the CO₂ absorption spectrum suitable

for modeling with the quasi-random transmission function (Goody, 1964). The essence of this model is that lines are placed at random with respect to frequency, implying a Poisson distribution of the spacing between neighboring lines. The well-developed theory of single-line models is then readily utilized to construct a band model with overlapping lines. The analytical form of the resulting model is given by

$$T_i(s_1 - s_2) = \exp \left\{ -\beta \delta e^{\delta} [I_o(\delta) + I_i(\delta)] \right\},$$

$$\delta \equiv S_o |s_1 - s_2| / (2\pi\alpha\rho_o)$$

$$\beta \equiv 2\pi\alpha/d \quad (17)$$

where:

S_i : average line intensity in
the i -th frequency interval

α : mean half width

d : mean line spacing

I_o, I_i : Bessel functions of the
first kind of imaginary
argument.

Prabhakara and Hogan (1965) have utilized the laboratory data of Stull, Wyatt and Plass (1963) to construct a representation of (17) for the carbon dioxide spectrum, assuming that gas-kinetic properties do not vary along the geometric path. The tabulated band parameters are given by $c_1 = S_o \rho_o / (2\pi\alpha_o)$, $c_2 = 2\pi\alpha_o / (\rho_o d)$.

With these parameters, the arguments of the function (17) may be calculated for non-standard pressure and temperature through the relations

$$\delta = \frac{c_1 \exp[\Gamma(T_0^{-1} - T^{-1})] P(s_1, s_2)}{P_0 P \sqrt{\frac{T_0}{T}}}, \quad \beta = c_2 P \sqrt{\frac{T_0}{T}}$$

The tabulated coefficient Γ accounts for the dependence of line intensity on temperature in the 15μ -band.

From (17) we may derive the following limiting forms:

$$\begin{aligned} T_i(s_1, s_2) &\rightarrow \exp(-\beta \delta), \quad \delta < 0.1 \\ T_i(s_1, s_2) &\rightarrow \exp[(2\pi^{-1}\beta^2 \delta)^{1/2}], \quad \delta > 3 \end{aligned} \quad (18)$$

These are the weak- and strong-line limits, respectively.

It must be stressed that (17) is valid for a path length of uniform gas-kinetic conditions. In the governing equations (7) and boundary conditions (8), the transmission function must be evaluated over extended path lengths, so that variations in pressure and temperature are significant. In the numerical model, this effect is approximated by dividing a given extended path into a number of shorter segments, within which the gas-kinetic conditions do not vary appreciably. The transmission functions for each of these segments are then calculated, and their

product is used to approximate the transmission of the extended path.

For a given spectral interval and geometric path length, either the weak- or strong-line forms of (17) is used, depending on the value of δ for the particular calculation.

In those atmospheric strata assumed to be dust-laden, the gaseous transmission is reduced by a factor $\exp(-\beta^d \Delta x)$, where β^d is an "effective absorption" coefficient due to dust, and Δx is the thickness of the layer.

3.2 Finite-Difference Form of the Governing System of Equations

The system (7) through (10) must be put into a form suitable for computational analysis. The basic procedure is to approximate the integrals in (7) and (8) by quadrature formulae, and the differentials by finite differences. It should be recalled that integration over the zenith angle has been performed implicitly by introduction of the "diffusivity factor" b (eq. (13)).

As discussed in Section 3.1, integration over frequency is approximated by summation over a number of frequency intervals embracing the 1-6 and 12-18 μ vibration-rotation bands of carbon dioxide. The CO₂ band parameters and raw solar spectral intensities are presented by Pallmann (1968). 62 increments of approximate width 50 cm⁻¹ are utilized, and the lower surface is assumed to be a "grey" emitter.

With the i-subscript referring to a frequency increment, (7a) and (8) take the form

$$\rho c \frac{\partial T}{\partial t} = \frac{\partial}{\partial x} \left\{ k \frac{\partial T}{\partial x} + 2\pi \sum_i [S_i(0) \mathcal{T}_i(x, \bar{\mu}) + G_i(x_s) \mathcal{T}_i[b(x-x_s)] - \int_0^x B_i(\xi, t) b' \frac{\partial}{\partial \xi} \mathcal{T}_i[b(x-\xi)] d\xi - \int_x^{x_s} B_i(\xi, t) b' \frac{\partial}{\partial \xi} \mathcal{T}_i[b(\xi-x)] d\xi] \Delta v_i \right\} \quad (19)$$

$$k_s \frac{\partial T_s}{\partial x} - k \frac{\partial T}{\partial x} - \epsilon \sigma T_s^4 (x_s - 0, t) + 2\pi \sum_i \left[\int_0^{x_s} b' B_i(s, t) \mathcal{T}_i[b(s-x_s)] ds' + (1-\alpha_s) S_i(0) \mu \mathcal{T}_i(x_s, \bar{\mu}) \right] \Delta v_i = 0 \quad (20)$$

Each of the transmission functions \mathcal{T}_i is approximated by a product, as indicated previously. For example, we may write

$$\mathcal{T}_i(x_1 - x_2) = \prod_{j=1}^J \mathcal{T}_i(x_j - x_{j-1}) \quad (21)$$

where the product index j extends over all J intervening segments $(x_j - x_{j-1})$ between the endpoints of depth x_1, x_2 .

Integration over the depth coordinate in (19) and (20) is represented by a summation over a number of atmospheric strata. For convenience, these strata are taken as the same ones used in the product algorithm (21). Using the subscript index m for a given level between the surface and 50 km, (19) and (20) assume the form

$$\rho_m c \frac{\partial T_m}{\partial t} = \frac{\partial}{\partial x} \left\{ k \frac{\partial T_m}{\partial x} + 2\pi \sum_i [S_i(0) \mathcal{T}_i(x_m, \mu') + b' G_i(x_s) \mathcal{T}_i[b(x_m - x_s)] \right. \\ \left. - \sum_{m=1}^M B_{i,m} b' \frac{\partial}{\partial \xi_m} \mathcal{T}_i[b(x_m - \xi_m)] \Delta \xi_m - \sum_{m=m}^M B_{i,m} b' \frac{\partial}{\partial \xi_m} \mathcal{T}_i[b(\xi_m - x_m)] \Delta \xi_m \right\} \Delta v_i, \quad (22)$$

$$k_s \frac{\partial T_s}{\partial x} - k \frac{\partial T}{\partial x} - \epsilon \sigma T_s^4(x_s, 0, t) + 2\pi \sum_i \left[\sum_{m=1}^M B_{i,m} b' \mathcal{T}_i[b(x_m - x_s)] \Delta x_m' \right. \\ \left. + S_i(0)(1 - \alpha_s) \mu \mathcal{T}_i(x_m, \mu') \right] \Delta v_i = 0 \quad (23)$$

Finally, the derivatives in (22) and (23) are replaced by finite differences. A simple forward difference is used for the time derivative, while modified centered differences are employed in the space derivatives. The resulting equations, including the product representation (21), are quite lengthy and will not be reproduced here. The corresponding finite-difference form of (7b) is

$$\rho_m c \frac{\overline{T}_{sm}^{n+1} - \overline{T}_{sm}^n}{\Delta t} = \frac{k}{(\Delta x)^2} (\overline{T}_{sm+1}^n - \overline{T}_{sm}^{n+1} - \overline{T}_{sm}^{n+1} + \overline{T}_{sm-1}^n), \quad m = M+1, M+2, \dots M_d \quad (24)$$

where the superscript refers to the timestep, and m_d is the lowest soil level under consideration. In (24), as well as the finite-difference form of (22) and (23), the Dufort-Frankel two-level explicit differencing scheme (Richtmyer and Morton, 1967) has been employed. This scheme is unconditionally computationally stable.

From (15) and (16), the finite-difference form of the internal boundary condition takes the form

$$k_s \frac{T_{SM+1}^{n+1} - T_{SM}^{n+1}}{\Delta x_s} - k \frac{T_{M-1}^{n+1} - T_M^{n+1}}{\Delta x_M} - 4\pi\sigma T_{SM}^n (T_{SM}^{n+1} - \frac{3}{4} T_{SM}^n) + \\ 2\pi \sum_{i=1}^m \sum_{m'=1}^n B_{i,m'}^n J_i^n [b(x_m - x_{m'})] \Delta x_{m'} + 2\pi \sum_i (1 - \alpha_s) S_i^n J_i^n (x_m \bar{\mu}') = 0 \quad (25)$$

Note that the soil surface temperature for the previous (n -th) timestep is used for the expansion (16). Again, the product algorithm (21) is used to evaluate each transmission function in (25). Each of the factors in the product is evaluated using the temperature distribution from the previous timestep.

We now turn to the question of the size of space and time increments to be used in the simulation. In view of the weak-and strong-line radiative transfer, we can expect a relatively complex atmospheric temperature profile, especially near to the surface, where large

temperature gradients will result in significant molecular thermal conduction. A reasonably high vertical resolution in the finite differencing is required to accomodate this feature, along with the requirement that temperature and pressure do not vary substantially over a given layer, so that the product algorithm (21) for the transmission function remains accurate. We have chosen 7 layers approximately logarithmically spaced in the lowest 1 km, and generally a 1 km spacing in the region between 1 and 50 km. A 2-cm increment was used for the subsoil layers.

From the estimates of Goody and Belton (1967), the characteristic time for relaxation of thermal perturbations having scales of the order of several meters is in the range of 10^3 sec for the Martian troposphere. On these physical grounds, we may infer that a computational time-step of similar size is required to adequately resolve in time the propagation of temperature waves in the near-surface layers. A 15-min time-step was used for all simulations reported in Section 4.

3.3 Input Data and Computational Procedure

The parameters and input data required for a given simulation are as follows:

- (1) initial distribution of atmospheric temperature, density, and subsoil temperature;
- (2) soil conductivity, density, and heat capacity, each assumed constant;
- (3) atmospheric conductivity and heat capacity at constant pressure;
- (4) soil surface albedo and emissivity;
- (5) CO₂ band parameters and solar spectral radiances for each frequency interval; and
- (6) orbital parameters relating to the Martian day under consideration, and latitude of simulation.

The time-variation of solar radiation entering the top of the atmosphere is computed from the relation presented, e.g., by Sellers (1965).

Thermal parameters of the soil material were derived through a parametric procedure, in which soil thermal inertia was adjusted until the amplitude of diurnal surface temperature variation matched that suggested by Mariner radiometric scans. Numerical values of input parameters for each simulation reported will be presented in Section 4.

The computational procedure followed for each simulation begins with the calculation of transmission functions, solar spectral radiance, and atmospheric spectral emission corresponding to the initial time and temperature distribution. These quantities are then combined to form the total (conductive-radiative) heating/cooling function represented by the right-hand-side of (19).

In addition, the downward radiative flux incident at the surface is calculated, as required in (25). Eqs. (9), (24) and (25) are then solved for the subsoil and surface temperature at the end of the first timestep, and the new distribution of atmospheric temperature is computed from (23), with the boundary condition (9a). This procedure generates the subsoil and atmospheric temperature distribution for the end of the first timestep. New solar radiances are then calculated for the advanced local time, and the new temperature field is used as initial data for the execution of the next timestep. In this manner, the procedure continues through the total interval of time desired for the simulation. In most numerical experiments, this interval corresponds to 24 Martian hours, or 96 computational timesteps.

In the cases where the lower solid surface is assumed to be solid carbon dioxide, the internal boundary condition (25) is replaced by the requirement that temperature remains fixed at the CO_2 - sublimation point. The subsoil temperature field is assumed isothermal, so (24) is no longer required.

In all, there are 82 computational levels and 62 frequency intervals considered for each timestep. On the CDC 3300, approximately 20 sec of computing time are required for each step in the forward time-integration.

4.0 Basic Numerical Experiments and Interpretation of Results

4.1 Description of Experiments

The results contained in this chapter are based on a series of time-dependent numerical simulations of the Martian thermal energetics. Emphasis is given to the effect of a uniform dust layer on the transfer of radiation. This scientific interest evolved from the observational evidence of Mariner 9. For the simulations considered, a comparison is made between the results for a pure CO₂ atmosphere and those for a partially dust-laden atmosphere. The midlatitudinal and polar conditions are parametrically represented in table I.

TABLE I

Parameter	Midlatitudinal-Experiments (Mariner 7) (Mariner 9)		S. Polar Region Experiments (Mariner 9)	
Initial data	S-band Mar 7	IRIS	IRIS	IRIS
Initial time	0300 hr	1900 hr	1300 hr	1800 hr
Season	N.H. Autumn	S.H. Sum.	S.H. Sum.	S.H. Sum.
Latitude	+38°	-38°	-80°	-80°
Declination	-8°	-23°	-23°	-23°
Surface albedo	0.25	0.25	0.45	0.30
Surface emissivity	0.90	1.0	0.90	1.0
Thermal conductivity, CO ₂ gas (cgs)	1.33×10^3	1.33×10^3	1.33×10^3	1.33×10^3
Soil thermal inertia (cgs)	5.90×10^5	5.90×10^5	—	5.90×10^5

The midlatitude simulations involve a dual structure in which the ground-atmosphere subsystems are coupled by an interface energy balance, thereby accounting for temperature variations in the soil. For the polar ice cap simulations, the temperature of the ice cap surface is held fixed at the sublimation temperature of CO₂. An additional simulation is reported for a frost-free lower boundary.

4.2 Results and Interpretation

In this section, the material will be divided into three categories, based on the initial input data used in the simulations. Due to the large volume of reliable information derived from Mariner 9, most of the statements to follow pertain to simulation results based primarily on Mariner 9 data.

4.21 Mariner 7 Midlatitudinal Experiment

Numerical results of the first simulation evolved from Mariner 7 initial input data, i.e., temperature & pressure as a function of altitude derived from the S-band occultation experiment. Calculated atmospheric temperature distributions in the lowest 400 m, at specified times during

the Martian day, are portrayed in Fig. 1. The curvature of these profiles indicates that molecular conduction produces cooling at 0400 LMT, warming at 0900, no change at 1400, and cooling once again after 1800 LMT. (Note the logarithmic height scale). A dual structure

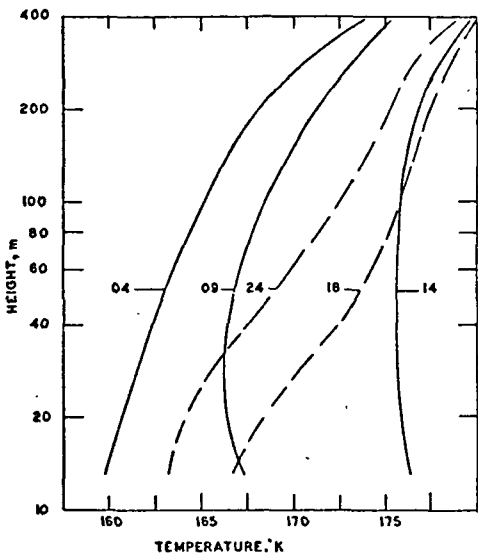


Fig. 1 Calculated temperature profiles in the lowest 400 m for various hours of the Martian Day.
Data: Mariner 7, mid-latitude (see Table I).

in the diurnal temperature wave propagation pattern is evident. One wave, primarily confined to the lowest 150 m, is superimposed on a second wave of larger characteristic

scale. Goody and Belton (1967) have predicted such a structure, based on the difference between time of relaxation of thermal perturbations by radiative and conductive processes in the Martian atmosphere. Their analysis indicates characteristic scales of 15 m and 1.5 km, respectively, for the molecular-conductive and radiative waves.

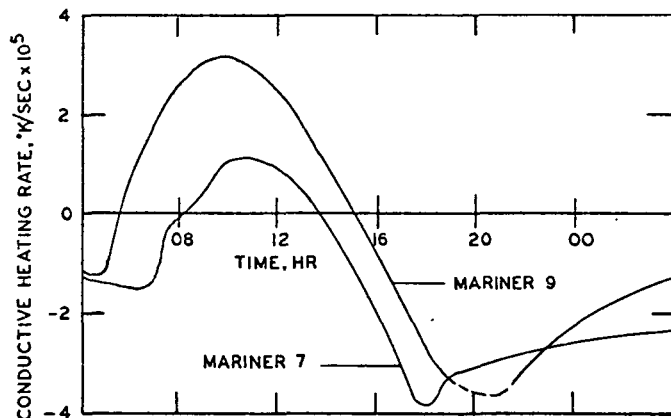


Fig. 2 Time-variation of molecular-conductive heating rate at the 12.5 m computational level, corresponding to the lowest 25 m layer.

Fig. 2 reveals the relative significance of atmospheric molecular conduction. At 1800 LMT, the conductive heating rate at the 12.5 m computational level reached $-3.9 \times 10^{-5} \text{ K sec}^{-1}$ (-3.4 K day^{-1}), representing 22% of the total (radiative-conductive) heating/cooling function.

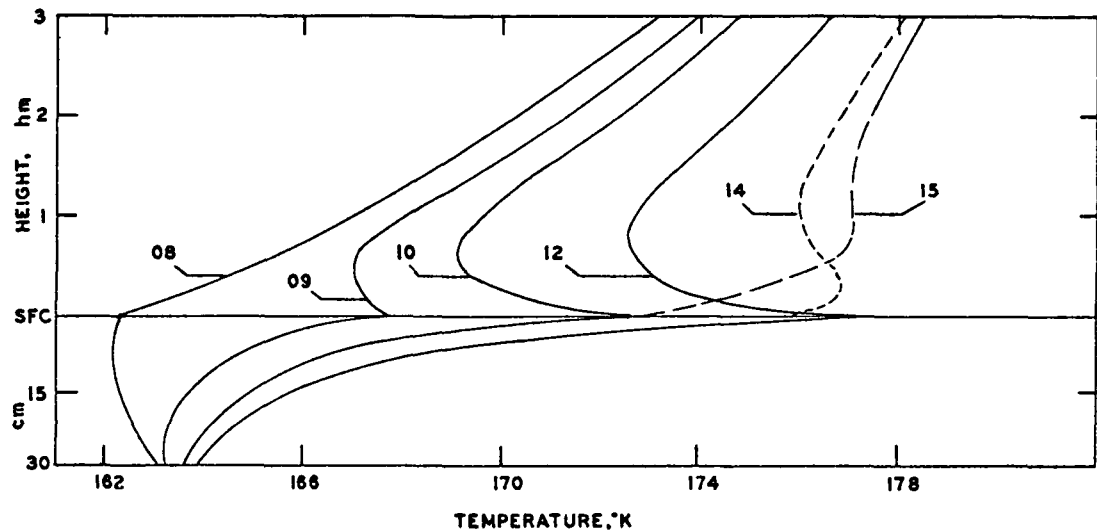


Fig. 3 Atmospheric and soil temperature profiles below 300 m (3 hm), showing evidence of dual-wave structure in thermal boundary layer. The subsoil temperature below 60 cm of depth is one of several simulation temperatures chosen.

In Fig. 3, the typical diffusion-like upward propagation of the perturbation at 0900 LMT may be traced through the profile for 1400 LMT when a second disturbance has been initiated by surface cooling. Again, an additional wave of larger scale is indicated, extending well into the region above 300 m.

4.22 Mariner 9 Midlatitudinal Experiment

The second simulation was conducted with the purpose of

investigating the effect of dust on the Martian thermal energetics. The results presented are based on two unique 24 hour simulative investigations.

The first case, designated "dust-free" utilizes, as initial data, the Mariner 9 IRIS inversion profile mentioned previously, with a local starting time of 1900 LMT. The second case used an identical initial sounding and starting time, but includes a simulated ground-based dust layer of 30 km thickness; this case will be termed "dust-laden".

Since over the night-time hours the radiative-conductive model is thermally dissipative, minor inconsistencies between the arbitrary subsoil and surface temperature and the atmospheric sounding tend to disappear over the night-time hours so that by sunrise, the entire temperature profile is thermally "initialized".

Fig. 4 depicts modeled atmospheric soundings for 0500 and 1600 LMT for each simulation. With regard to the dust-free case, basic regimes are evident. The lowest regime, from the surface to about 4 km, includes those atmospheric strata dominated by strong-line, short-path, diffusion-like radiative exchange associated with soil surface temperature variation. (This region actually

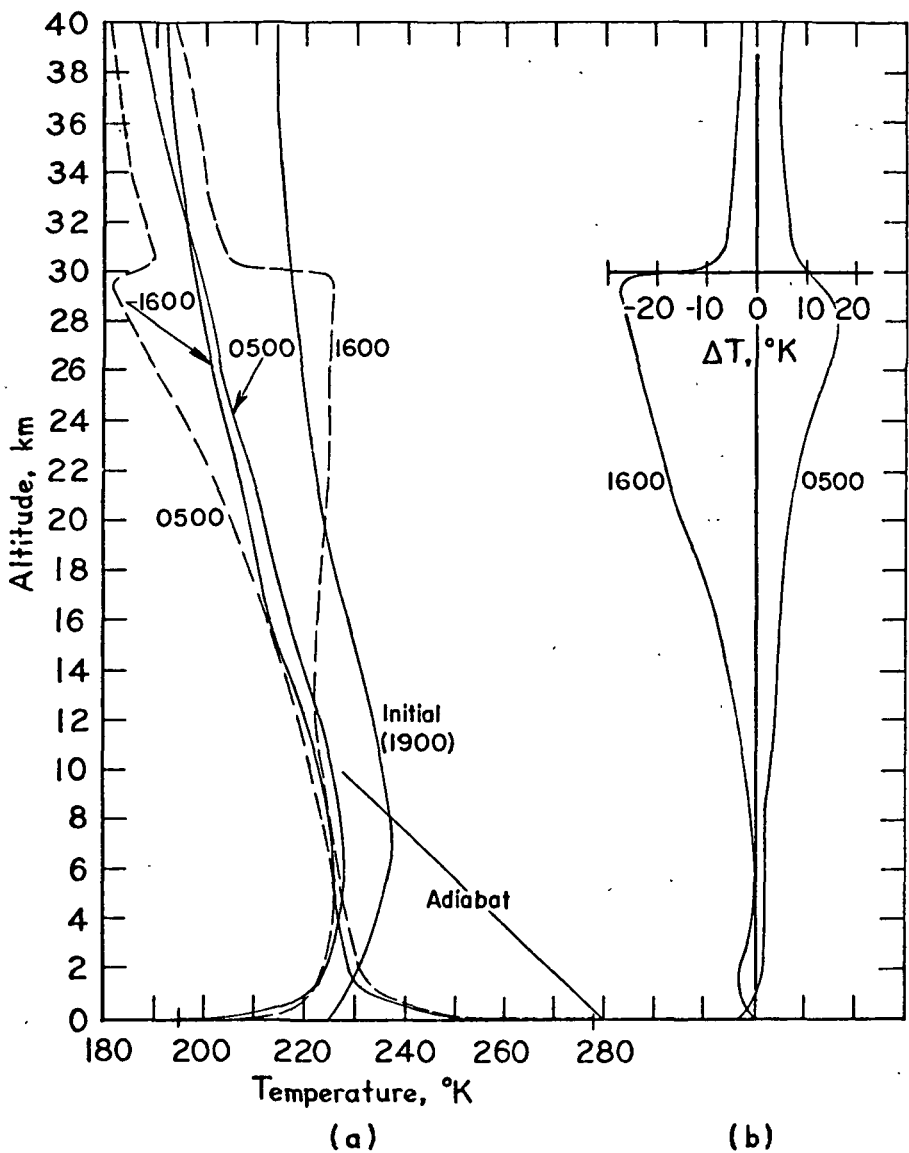


Fig. 4 (a) Modeled vertical temperature profiles at 0500 and 1600 local Martian time (LMT), for the dust-free (solid line) and dust-laden (dashed line) conditions. Also shown is the initial (1900 LMT) profile obtained from inversion (Hanel, et al., 1972) of Mariner 9 IRIS measurements by assuming a dust-free atmosphere. (b) profiles of the difference $\Delta T = T_c - T_d$ in temperature between the dust-free (subscript:c) and dust-laden (subscript:d) simulations, at 0500 and 1600 LMT.

exhibits a further fine structure, to be elucidated in conjunction with Fig. 2, which may be attributable to the diffusion-like dual action of molecular conduction and strong-line radiative transfer). The region between 4 and 31 km is directly affected by surface temperature variation primarily through weak-line exchange, but also undergoes direct solar heating and weak-line losses to outer space. The regime above 31 km is dominated by the upper boundary conditions, i.e., direct solar heating and emission to outer space, and is affected little by soil surface temperature variation, which lags solar forcing by roughly 4 hours.

Soundings of the dust-laden case exhibit essential differences from those of the dust-free simulation primarily in the middle regime (4-31 km). Over the daylight hours, this region approaches an isothermal stratification, in agreement with recent Mariner 9 findings showing a tendency towards this structure in the dust-laden mission phases. The top of the dust layer acts as an "effective radiation surface", similar in its radiative impact to the solid soil surface. Diurnal temperature variation at the top of the dust layer is nearly 50% of the amplitude of surface temperature variation. Thus, the upper regime (above 31 km) responds to this effective radiation table in the same

way as the lowest regime responds to surface temperature variation in the dust-free case. A statically-unstable layer is generated at the top of the dust layer in the afternoon hours.

The initial (1900 LMT) Mariner 9 IRIS profile was derived by inverting the IRIS radiance measurements obtained during a dust-laden mission phase, to generate an emission profile, assuming a dust-free atmosphere. As indicated in Fig. 4, the profile approximates a smoothed version of the modeled 1600 LMT output for the dust-laden simulation, with decreasing fidelity towards the surface.

The curves in the right-hand portion of Fig. 4 show profiles of the difference in temperature between the dust-laden and dust-free simulations, at 0500 and 1600 LMT. At 0500, the dust-laden profile is warmer than the dust-free in the lowest 400 m, an indication of the shielding effect of the dust blanket keeping surface temperature slightly higher in the nocturnal hours. However, in the bulk of the dust layer, a cooling has occurred by 0500 LMT which is substantially larger than in the dust-free case. This is attributable to the simulated "grey-body" emission of the dust particles, which results in more non-absorbed photons being emitted per unit volume from a dust-laden layer than from the same layer under dust-free conditions.

Atmospheric and subsurface temperature profiles in the layers near the interface are shown in Fig. 5, for the dust-free case. The basic structure of the subsurface profiles reflects the relatively large soil thermal conductivity (2.3×10^5 erg cm $^{-1}$ sec $^{-1}$ K $^{-1}$) used in the simulation, modeling low-porosity silica.

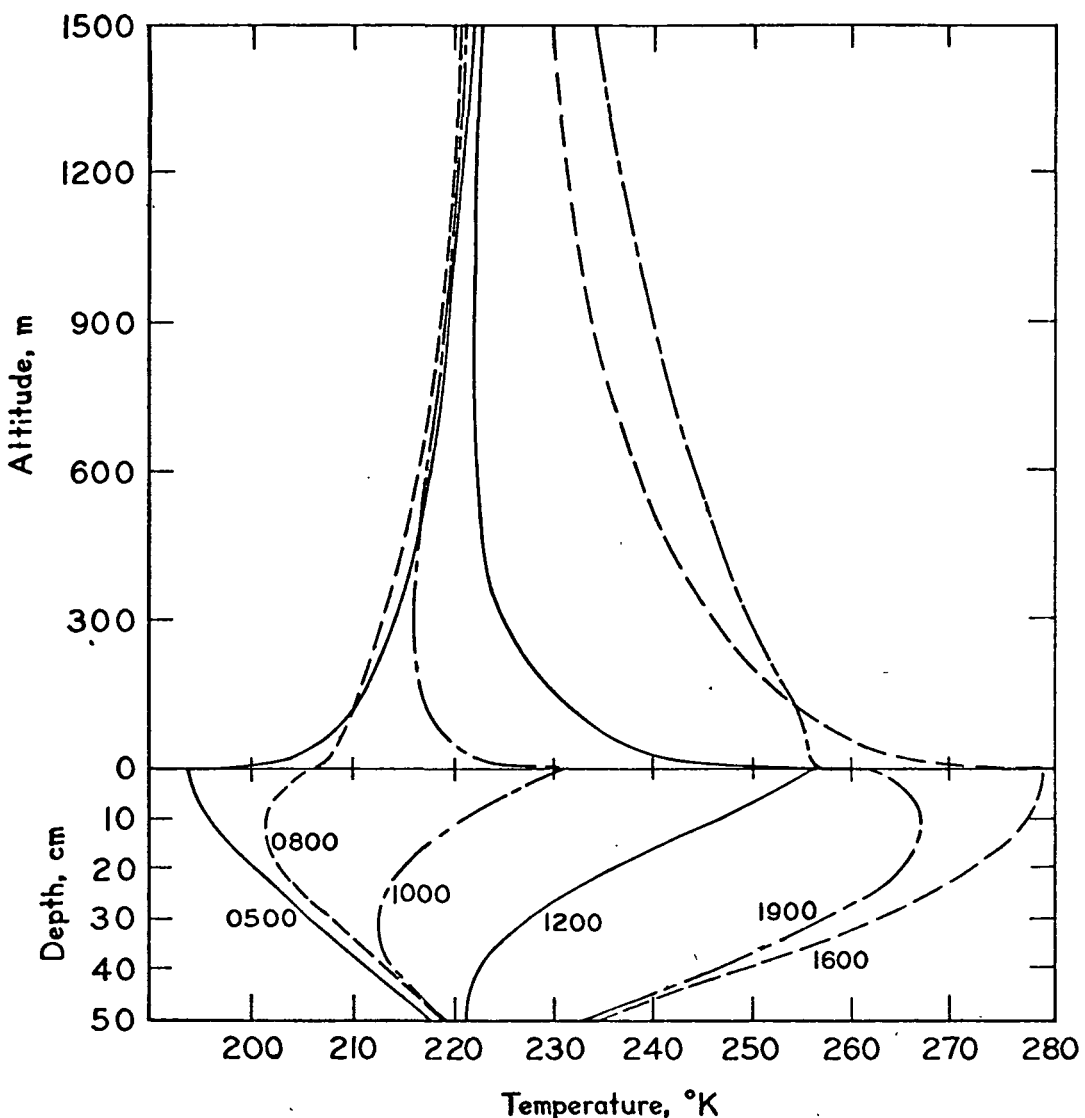


Fig. 5 Vertical temperature distributions in the sub-soil and lower atmospheric layers for selected hours of the Martian day, from the dust-free simulation. For environmental parameters used, see table I.

The atmospheric profiles exhibit diffusion-like heat transport characteristics, due to the dual action of strong-line radiative and molecular-conductive transfer. An "effective radiative-conductive diffusivity" may be estimated by L^2/τ where L and τ are the characteristic length and time scales of the diffusion process. This diffusivity is found to be $\sim 2 \times 10^5 \text{ cm}^2 \text{ sec}^{-1}$, on the basis of data represented in Fig. 5. This compares well with Gierasch and Goody's (1968) scaling estimate of $10^5 \text{ cm}^2 \text{ sec}^{-1}$, and is similar in order-of-magnitude to a free-convective eddy diffusivity under mildly-unstable conditions. This also tends to corroborate Goody and Belton's (1967) estimate that the time for the relaxation of thermal perturbations by radiation and mild turbulent convection should be comparable for a perturbation length scale of hundreds of meters.

In Fig. 6, each of the various heat flux components acting at the soil-atmosphere interface are shown as a function of the time of day. Short-term oscillations of decreasing amplitude, evident in the first two hours of the simulation, represent the dissipative smoothing of inconsistencies in the arbitrary initial temperature distribution in the interface and subsurface layers.

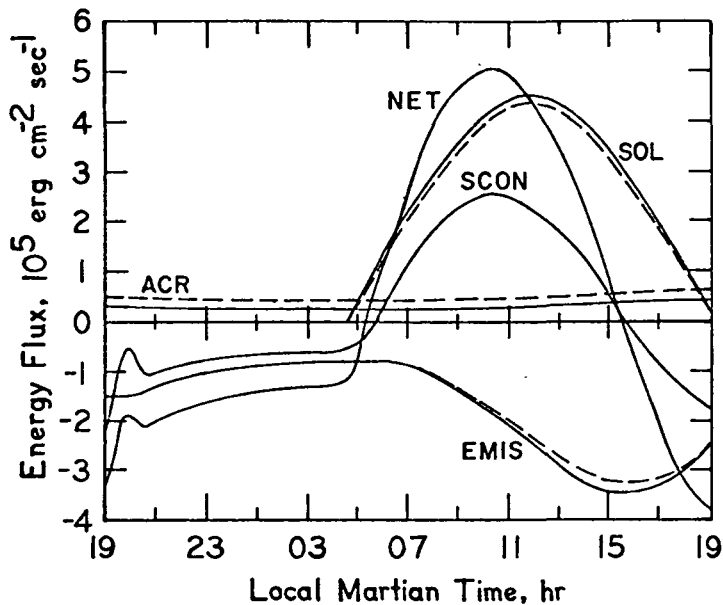


Fig. 6 Diurnal history of the various component heat fluxes at the soil atmosphere interface. EMIS represents the flux of long-wave radiation emitted by the surface, SCON the molecular-conductive heat flux in the soil material, SOL the absorbed insolation, ACR the absorbed flux of atmospheric counter-radiation, and NET the algebraic sum of all component heat fluxes. Solid lines depict results for dust-free conditions, while the dashed lines (shown for EMIS, SOL, and ACR only) relate to the simulated dust-laden conditions. Influence of CO_2 -gas thermal conduction is of lesser significance at the interface, and curve is not shown.

The fact that the model does not reproduce after a cycle of 24 hours the initial flux values can be traced to at least two possible causes. The most obvious is the lack of the model to account for removal of heat from the interface layers by mechanical and/or thermal convection

after a statically-unstable temperature distribution has been generated by surface radiative heating. However, it is also possible that the initial atmospheric temperature profile may not be representative of the local time and season relevant to the IRIS measurement on which the inverted sounding is based. The preliminary Mariner 9 sounding utilized was based on an inversion method which assumes a dust-free atmosphere.

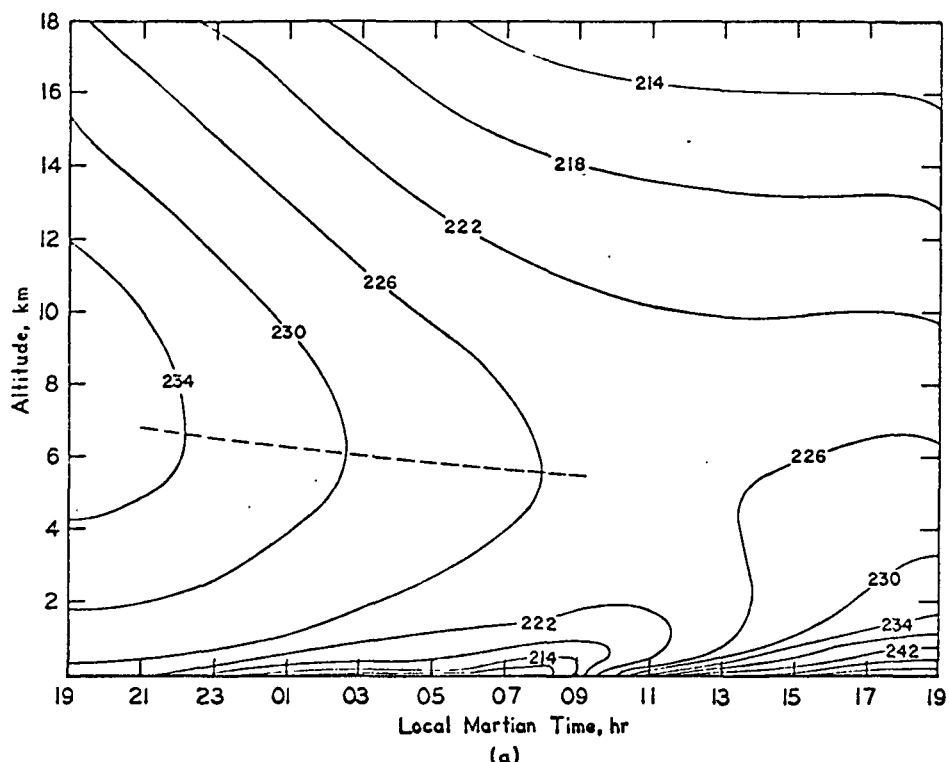
Molecular-conductive heat flux in the soil material is a significant fraction of the net flux available for temperature changes, at all times during the 24 hr simulated period. The conductive flux reaches a maximum about 1.5 hours before local noon, in agreement with measurements under comparable terrestrial physical settings (Sellers, 1965).

Planetary atmospheric "counter-radiation" varies little over the diurnal cycle. Since the concentration distribution of radiatively-active gases remains constant in the model, any temporal variation in counter-radiation can be traced directly to variations in the temperature distribution, for the dust-free case. The addition of a simulated dust layer, assumed a grey emitter in the CO₂ absorption bands, results in an increased counter-radiation for all times

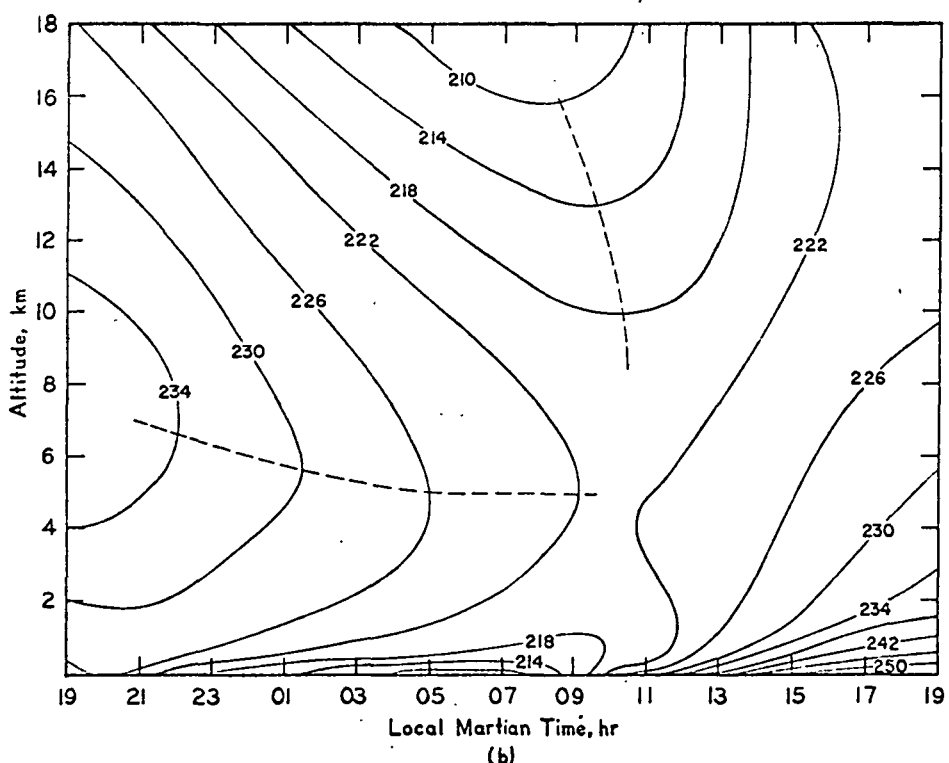
of the day, as evidenced in Fig. 6. This phenomenon accounts for a higher minimum morning temperature of 198K for the dust-laden case, as compared with 193K for the dust-free simulation.

Height-time cross sections of the temperature field in the lowest 18 km are shown in Fig. 7. Qualitatively, the pattern is nearly unchanged by the presence of dust, in the lower 4 km. As discussed earlier, this region responds primarily to changes in the interface temperature, and variation of the latter quantity is not significantly modified by the presence of the dust layer (cf. Fig. 6, EMIS-curves).

The region above 4 km is modified drastically by the dust layer during the daylight hours. This regime responds to direct solar heating and, to a lesser extent, to interface-temperature variation. The dust-laden layers above 7 km develop a nearly isothermal stratification in the afternoon hours, in agreement with recent Mariner 9 observations (JPL, 1972).



(a)



(b)

Fig. 7. Height-time cross-sections of the modeled temperature field (deg. K) in the lowest 18 km for (a) dust-free, and (b) dust-laden conditions. Approximate extremal lines are dashed.

4.23 Mariner 9 South-Polar Region Experiment

The final portion of Section 4 consists of the simulative results for the Martian polar region. The essential characteristics of the atmosphere and ground environment are displayed in Fig. 8. Due to the tenuity of the Martian atmosphere, incoming solar radiation may be considered as beam radiation diffusely reflected by

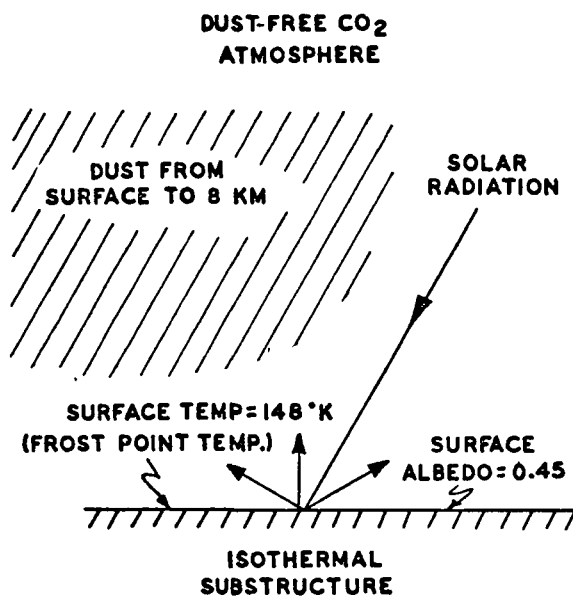


Fig. 8 Schematic physical setting of the south polar ice cap region. Hatched area depicts extent of dust layer from surface to 8 km. Solar radiation is diffusely reflected at the ground; albedo value of .45 represents condition of CO₂ frost surface in interaction with solar spectrum up to 5 μ .

the surface. At the dry ice surface, the frost point temperature of CO₂ is the equilibrium temperature for the solid and gaseous phases. Therefore, the thermal condition at the interface was permanently fixed at 148K with an isothermal substructure. Further details are presented in Pallmann and Frisella (1972).

Mariner 9 measurements support the assumption that a dust layer of moderate optical thickness extended from the ground to about 8 km. In the model a value of the effective infrared optical thickness due to dust $\gamma_{IR}^d = 1.6$ was assumed for dust-laden simulations. The initial input data was derived from the inverted Mariner 9 IRIS data (temperature and pressure), pertinent to 1300 LMT over the south polar cap region. This temperature distribution together with the thermal structures 24 hours later, for both clear and dusty cases, are portrayed in Fig. 9. These distributions have been plotted only up to 15 km. Several noteworthy characteristics can be commented upon, foremost is the overall cooling at all levels. In the initial sounding, 12.5 km corresponds to the height of the maximum temperature occurrence; however, 24 hours later for both the dust and clear distributions the maximum temperature of the sounding occurred at the 7.5 km level. Below 8 km, the effect of the presence of dust seems evident. At first glance, a maximum cooling of approximately 11K in the region between 1.5 and 3.5 km is discernible.

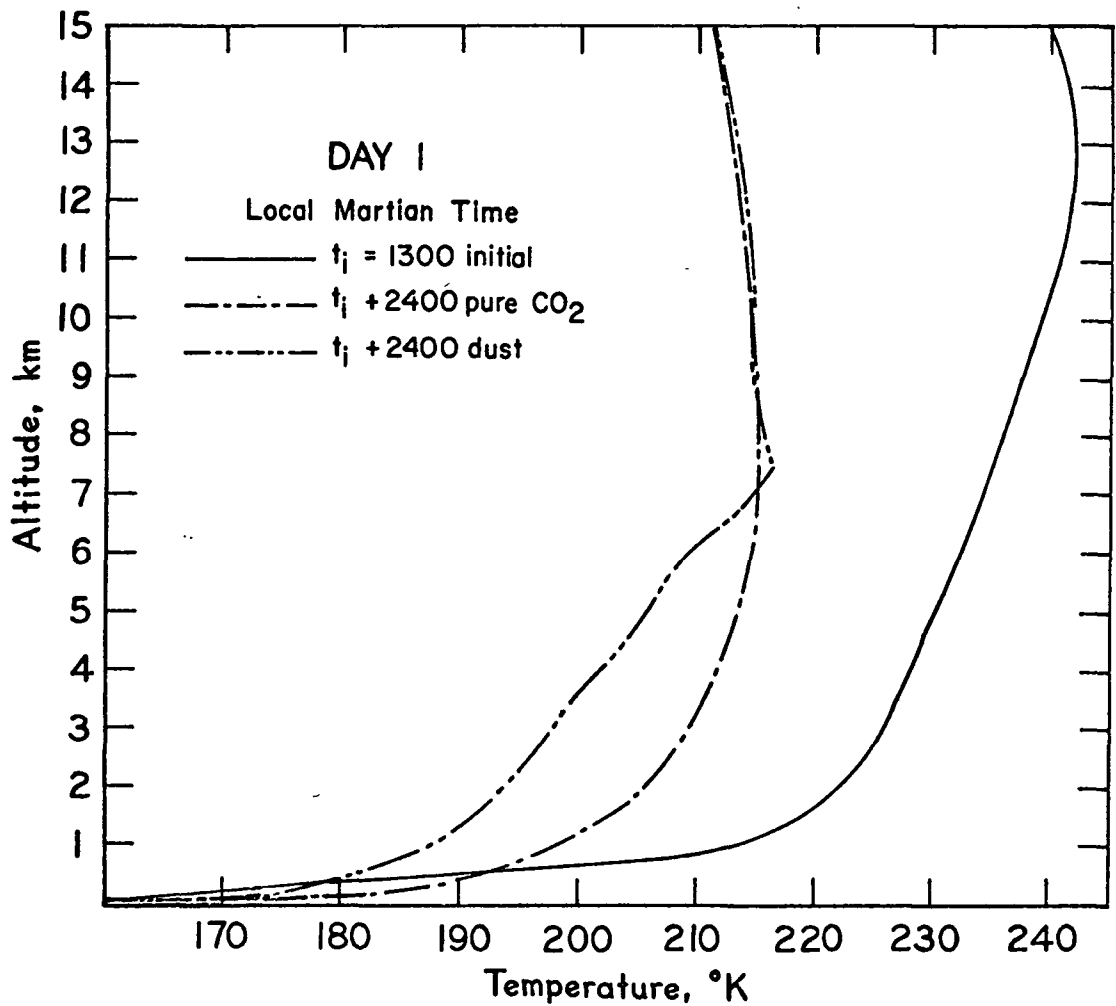


Fig. 9 Temperature profiles for Day 1 (0-24 hr) simulation. Solid line depicts the initial Mariner 9 IRIS inverted data, the 'dash-dot' represents the prognostic 24 hours calculated profile for a pure CO_2 atmosphere, and the 'dash-dot-dot' portrays the corresponding profile for a dust-laden simulation. All curves converge to 148K at the surface.

Upon closer examination of the output, it became clear that the cumulative source layer radiative flux was larger in magnitude than the incoming solar flux, as can be seen in Fig. 10. This indicated that the temperature profiles were adjusting themselves toward a quasi-oscillatory thermally-

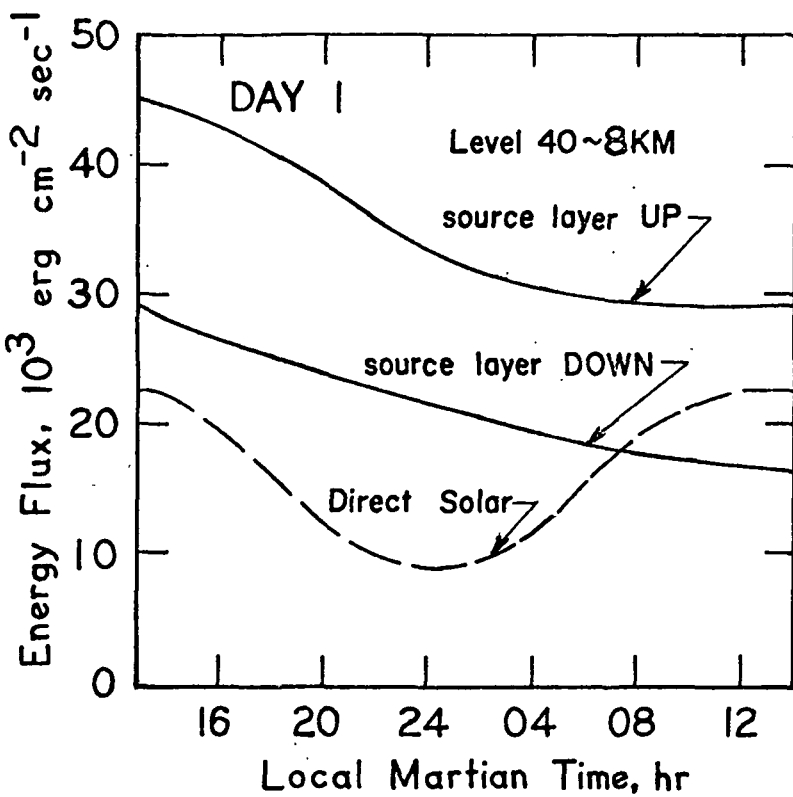


Fig. 10 Energy flux as a function of time (LMT) at the top of the dust layer (level 40). Source layer up, source layer down, and direct solar represent the upwardly- and downwardly-directed cumulative atmospheric radiative fluxes and downward direct solar radiative flux, respectively, at level 40.

balanced distribution. The simulation was therefore extended out in time another 24 hours, utilizing the final sounding of Day 1, as initial input data. Fig. 11 represents the resulting temperature distributions for the second day of simulation. Once again, the maximum temperature occurred at 7.5 km. Most importantly, a thermally balanced profile was established, as evidenced by the warming between the 4 and 8 km, comparing the 0600 LMT and the final 1300 LMT outputs.

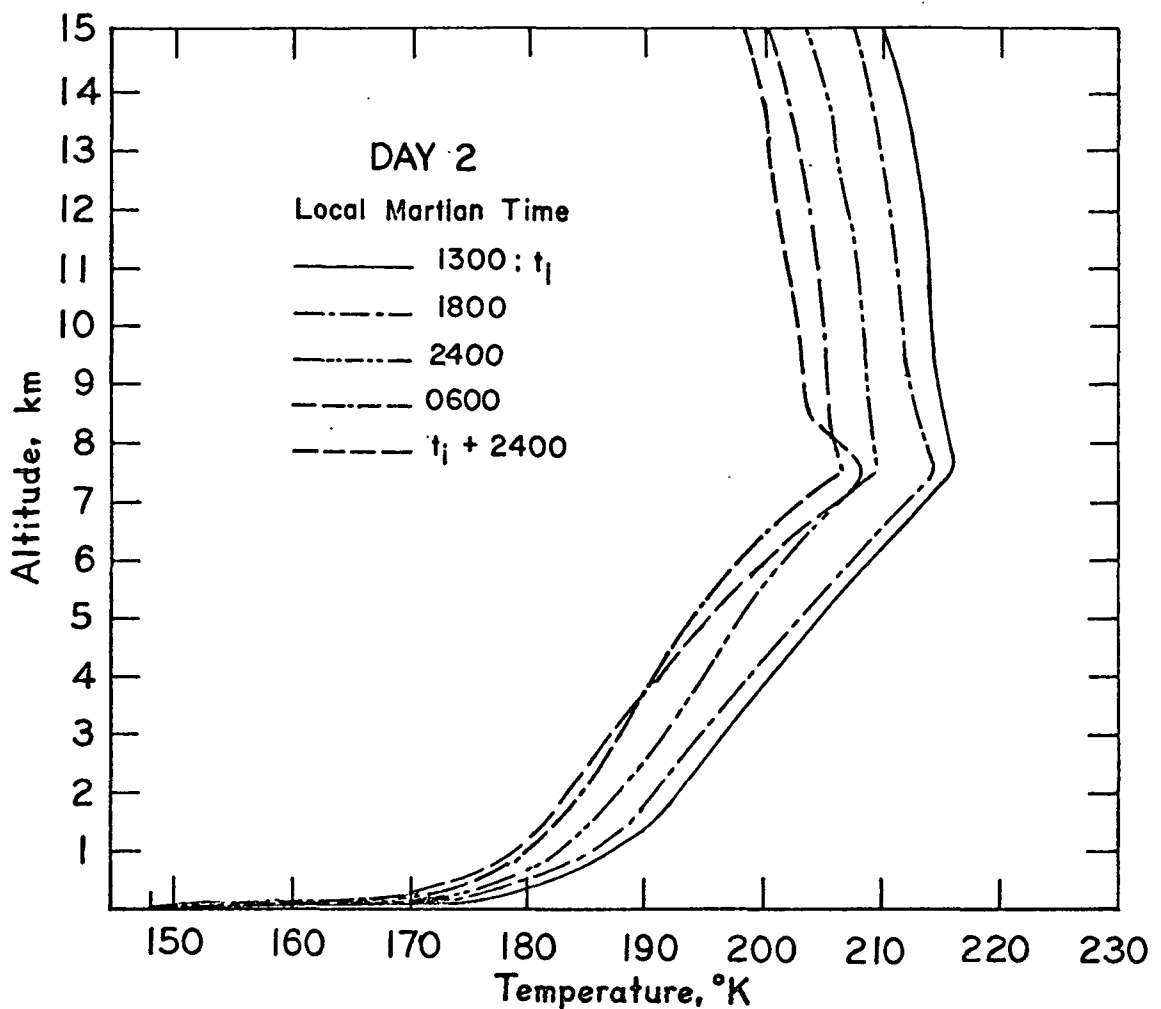


Fig. 11 Temperature profiles of Day 2 (24-48 hr) for the dust-laden simulation. Solid line depicts the final temperature sounding from Day 1 simulation used as initial data t_i ; also depicted are the 1800, 2400, 0600 LMT and the final ($t_i + 2400$) soundings.

The simulation was extended another 24 hours as depicted in Fig. 12. Comparing the initial IRIS inverted sounding with the 72 hour simulated temperature distribution reveals a substantial cooling of about 35K at all levels. Also indicated is the existence of a super-adiabatic layer between 7.5 and 8.5 km. It should be noted that the integral in-

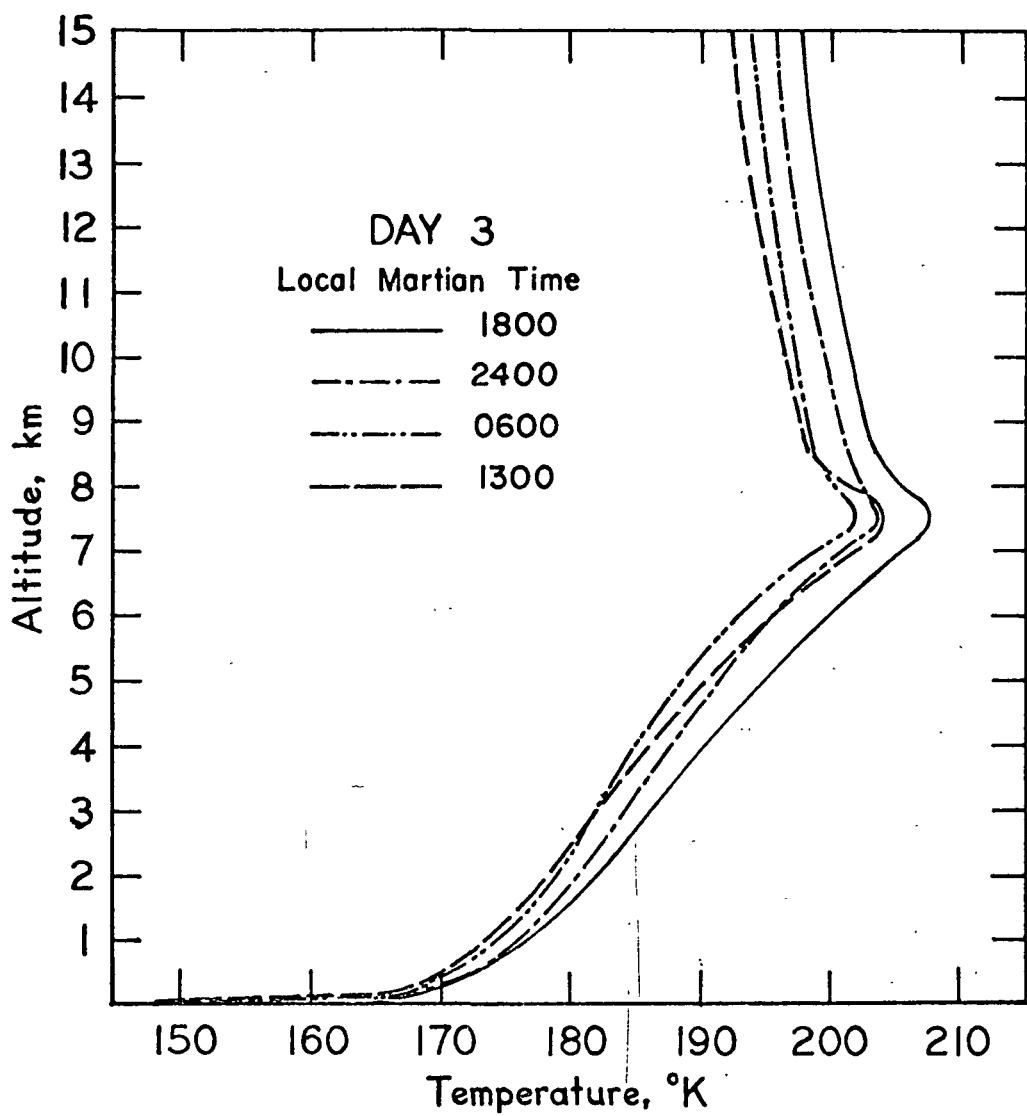


Fig. 12 Temperature profiles at Day 3 (48-72 hr), for the dust-laden simulation, which started at 1300 LMT.

version of the Mariner 9 IRIS signals was based on an algorithm for dust-free conditions. This could explain part of the simulated cooling. It is also possible that another non-simulated physical transfer mechanism could reduce the degree of cooling.

The constant ice cap temperature constraint imposed in our simulation permits the existence of a radiative sink phenomenon. The emission by the warmer atmospheric layers, varying between 1.7×10^4 and 1.3×10^4 erg cm $^{-2}$ sec $^{-1}$ for Day 1, initiates a downward heat flux onto the CO₂ ice cap surface.

These simulations do not directly require an accounting of incoming solar energy flux over all spectral wavelengths. The effect of this added energy source should have the following repercussions:

- (1) a percentage of the total incoming solar flux will be conducted into the ice cap, causing corresponding temperature changes to occur;
- (2) a fraction will be used in the initiation of phase changes (solid CO₂ to gaseous CO₂) and the resultant CO₂ mass transfer by diffusion in the vertical will alter the vertical density distribution and also the thermal energetics;
- (3) a fractional amount of the incoming solar radiation, will be attenuated through absorption and scattering, by the dust layer and may contribute to warming.

The possibility remained that the Mariner 9 IRIS data was obtained over a frost-free region. To gain deeper insight into such a situation, another simulation was conducted with due consideration given to the interaction between

the ground and atmosphere. Fig. 13 depicts the dust-laden 1800 LMT initial temperature sounding adjusted to a surface temperature of 230K, together with the

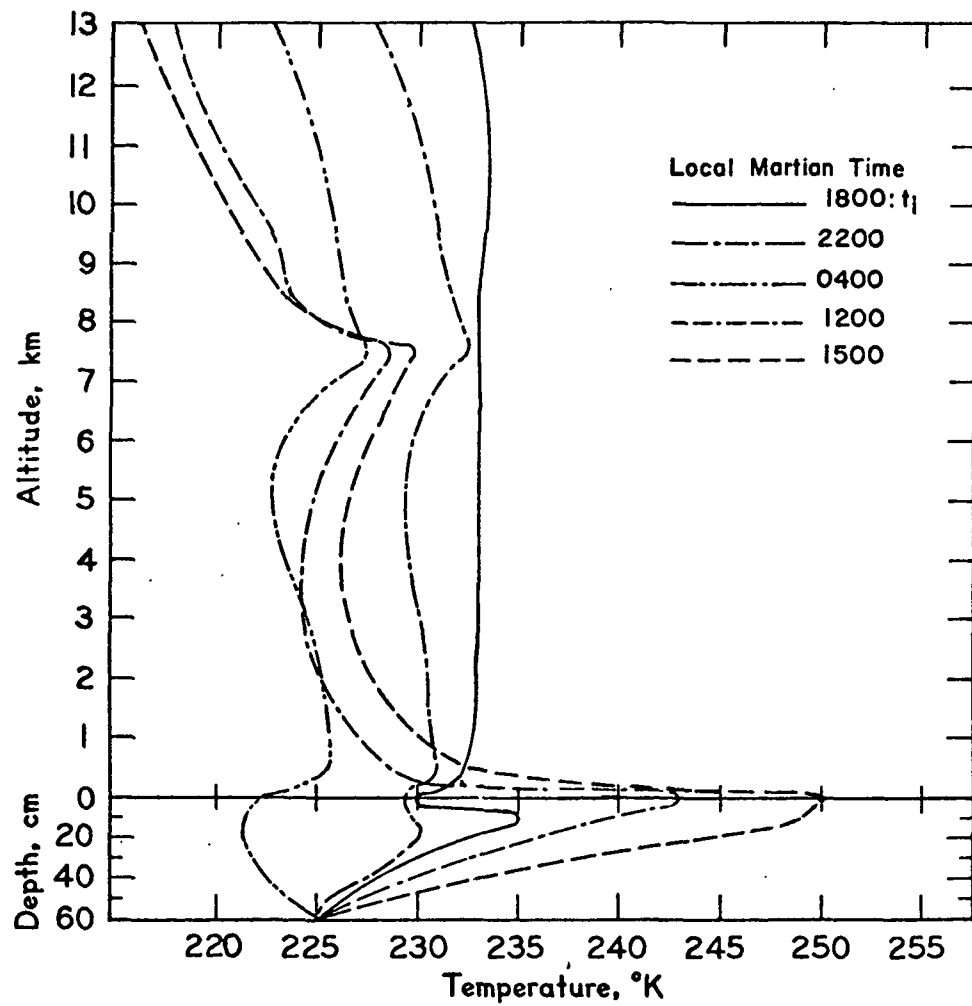


Fig. 13 Atmospheric and soil temperature profiles as a function of the hour (LMT) for a frost-free sand surface at 80° S; t_i specifies the time of the initial sounding.

initial soil temperature profile extending to a depth of 60 cm. The results of a 24 hour simulation reveal a substantially-reduced overall layer cooling, except for the region above the dust layer. The magnitude of cooling above 8.5 km is markedly lower as can be seen by comparison with the soundings in Fig. 9.

The effect of a thermally-conductive soil interacting with the lower polar atmosphere substantially alters the atmospheric thermal structure. A strong super-adiabatic layer extending from the surface to about 425 m is evident at 1130 LMT; by 1530 LMT this layer had expanded to the 800 m level. The effect of the dust layer is seen by comparing the 0400 LMT with the 1500 LMT soundings. Warming is observed below 7.5 km, while cooling occurs above. Between 7.5 and 8.5 km, a super-adiabatic temperature distribution is first noted at 1330 LMT. This layer remained super-adiabatic throughout the rest of the simulation due to the inability of the model to account for convective adjustment. These simulative results support the following tentative conclusions:

- (1) the condition of the lower boundary surface, soil versus solid CO₂, substantially alters the thermal energetics in the adjacent atmosphere,

- (2) this distinction must be taken into consideration for any investigation of the vertical structure of temperature utilizing the integral inversion technique; for this effect may be as important to the derived inverted temperature profile as the presence of dust particulates, and
- (3) a more refined simulation model incorporating the effects of solid CO₂ molecular thermal conduction, phase change, sublimation and vertical mass diffusion, should be developed for the polar frost cap region.

5.0 Theoretical Framework of the Generalized Problem

5.1 Background & Orientation

In the areas of non-LTE radiative transfer and local thermal energetics simulations, considerable developments have separately been achieved. This section of the report presents a detailed synthesis toward a rigorous remodeling program.

The most direct impact of a dust storm on the radiation field of the atmospheric boundary layer is through 1) the existence of scattering and absorbing aerosol, 2) the close proximity of a lower boundary with specific radiative characteristics, and 3) the strong variation of the absorptive and emissive powers at the top of the dust layer. The implication of 1) is that a rigorous modeling of radiative transfer is required which must include the formalism of non-conservative multiple Mie scattering by haze layers in the context of an inhomogeneous structure of atmospheric stratification. The interaction of the radiation field with the particulates as well as with the CO₂ molecules controls the radiative heating/cooling rate. The mathematical treatment must consider polarization, in which case the equation of transfer is replaced by a matrix equation (Busbridge, 1960).

The solution of the matrix integro-differential equation of transfer has been discussed by e. g., Adams & Kattawar (1970; "invariant imbedding" approach), Hanson (1969, 1971; "doubling method"), and Herman and Browning (1965; modified Gauss-Seidel iteration). Bergstrom (1971) and Dave (1970) showed the iterative method to be sufficiently flexible.

Shahrokhi and Wolf (1968) applied a finite difference scheme to the local integro-differential equation of radiative transfer. The Gauss-quadrature approximation of the source function integral yields a system of ordinary differential equations which lend themselves to finite difference evaluation by direct iteration.

The integration of the phase function and the scattering and extinction coefficients has most often been accomplished by using the modified gamma size distribution for the particulate polydispersion (Dave, 1969; Deirmendjian, 1969). Some information for fitting this distribution is available in the IRIS and other measurements of Mariner 9.

Construction of the atmospheric thermal energetics simulation involves the calculation of radiative, conductive and convective heat flux divergences throughout the atmospheric layer structure, and the formulation of the balance of component fluxes at the interface between the

Martian soil and the overlying atmosphere. The resulting non-linear integro-differential energy balance equation must then be solved for the temperature as a function of time and space.

5.2 Basic Definitions and Fundamental Relations of Radiative Transfer

For detailed derivations of fundamental radiative transfer equations, we refer to the standard works (Chandrasekhar, 1960; Preisendorfer, 1965). In this section, the matrix relations will simply be listed, with some relevant remarks.

Sekera (1963) has provided the local form of the equation of radiative transfer appropriate to the prototype problem: *

$$\frac{\mu}{\rho} \frac{d\mathbb{I}_v}{dz} = -[K_v^a(z) + K_v^s(z)] \mathbb{I}_v(z; \mu, \phi) + K_v^s(z) \mathbb{I}_s(z; \mu, \phi) + K_v^a(z) \mathbb{B}_v(z) \quad (26)$$

with $\mathbb{I}_s(z; \mu, \phi) = \frac{1}{4} \underline{\underline{P}}(\mu, \phi; \mu_0, \phi_0) \cdot \underline{F}_v \exp(-\tau/\mu_0)$

$$+ \frac{1}{4\pi} \int_{-1}^{+1} \int_{0}^{2\pi} \underline{\underline{P}}(\mu, \phi; \mu', \phi') \cdot \mathbb{I}_v(z; \mu', \phi') d\mu' d\phi' \quad (27)$$

*Bold-face letters denote column matrix (e.g., \mathbb{I}_v), and underscored letters denote 4×4 matrices (e.g., $\underline{\underline{P}}$).

In the above: $\mathbb{I}_v(z; \mu, \phi)$:Matrix of Stokes parameters representing the diffuse radiation field for depth z , zenith angle $\text{arc}(\mu)$, and azimuth ϕ ;

ρ :mass density

K_v^a :mass absorption coefficient

K_v^s :mass scattering coefficient

\mathbb{B}_v :matrix of Stokes parameters representing the unpolarized true emission;

\mathbb{P} :normalized phase matrix for the direction pair $(\mu, \phi; \mu', \phi')$.

Diermendjian (1969) and Samuelson (1965) have shown that the phase matrix may be factored into a product of a scalar function depending on the size spectrum and number density of scattering centers, and a matrix containing only angular dependence. Similarly, the appropriate mass absorption and scattering coefficients may be derived for a heterogeneous polydispersion by a suitable averaging process. It is assumed that such operations have been performed in (26), (27), and subsequent relations. Introducing the total thickness,

$$\tau_v = \int_{-\infty}^{z} [K_v^a(\xi) + K_v^s(\xi)] \rho(\xi) d\xi \quad (28)$$

and albedo for single scattering,

$$\omega(\tau_v) = K_v^s / (K_v^s + K_v^a) \quad (29)$$

(26) and (27) may be recast as

$$\begin{aligned} \mu \frac{d\mathbb{I}_v(\tau_v; \mu, \phi)}{d\tau_v} = & \mathbb{I}_v(\tau_v; \mu, \phi) - \omega(\tau_v) \left\{ \frac{1}{4} \mathbb{P}(\mu, \phi; -\mu_0, \phi_0) \cdot \mathbb{F} e^{-\tau_v/\mu_0} \right. \\ & \left. + \frac{1}{4\pi} \int_{-1}^{+1} \int_0^{2\pi} \mathbb{P}(\mu, \phi; \mu', \phi') \cdot \mathbb{I}_v(\tau_v; \mu, \phi') d\mu' d\phi' \right\} - [1 - \omega(\tau_v)] \mathbb{B}_v(\tau_v) \end{aligned} \quad (30)$$

In contrast to the local form of the radiative transfer equation, global formulations have been developed resting on optical properties of a finite mass of atmospheric layer material. Conventionally, transmission and scattering matrices are defined (Chandrasekhar, 1960; Sekera, 1963, 1966). The global point of view, which proved to be very successful in treating astrophysical systems, is only of limited value in the problem area of interface and boundary layer transfer. Therefore, its theoretical formulation and computational treatment will not be presented here.

For the intensity matrix, boundary conditions must be defined which are given here in the standard form:

$$\begin{aligned} \mathbb{I}_v(0; -\mu, \phi) &= \mathbb{I}_v^*(0; -\mu, \phi) = 0 \\ \mathbb{I}_v(\tau_t; \mu, \phi) &= \mathbb{I}_v^*(\tau_t; \mu, \phi) = 0 \end{aligned} \quad (31)$$

The asterisk denotes quantities referring to illumination from below. As explained by Chandrasekhar (1960), solutions to the "planetary problem" (i.e., that with a reflecting lower boundary) can be expressed in terms of the solution to the standard problem, by linear superposition

and slight modification of the matrices. Similarly, the effect of true emission at the lower boundary may be accomodated by adding an appropriate unpolarized isotropic intensity component to the upward intensity at the lower surface.

5.3 Solution of the Local Radiative Transfer Equation

An examination of the local radiative transfer equation reveals basically two solution approaches, depending on the choice of the dependent variable. If we choose the spectral specific intensity, then (26) is an integro-differential equation in which the angular variables appear as parameters. On the other hand, we can use the transfer equation to eliminate the intensity matrix from the source function definition (27) in which case the so-called auxiliary equation is generated. In the latter relation, the source function plays the role of dependent variable.

The auxiliary equation is of considerable theoretical utility, particularly for existence and uniqueness proofs, but has found computational use only in certain restricted contexts. These special cases are beset with many of the difficulties encountered with the global methods, because they were developed primarily for isotropic or Rayleigh

phase matrices. For these simplified scattering problems, the governing auxiliary equation becomes the familiar Milne equation (or, a simple variant of this form). The solution technique usually employed is the Neumann series (Busbridge, 1960; Dave, 1964, 1965; Irvine, 1968; Preisendorfer, 1965).

Many results have been obtained for multiple Rayleigh scattering problems, for which it can be shown that higher order terms in the Neumann series correspond to successively higher orders of scattering (Dave, 1964). As might be expected, the extension of these analyses to the context of non-conservative Mie scattering is not at all apparent. Furthermore, convergence of the successive approximations is very slow for moderate optical thicknesses.

Herman and Browning (1965) were among the first to regenerate interest in the fundamental local radiative transfer equation, and appeal to a well-known iterative approach for its solution. It represents a true departure from the restrictive confines of the astrophysical setting, is well-suited for simulation on a digital or analog computer, and yields directly the vertical distribution of spectral specific intensity, rather than the reflection and transmission matrices for a single optical depth. In principle, the approach is suitable for an arbitrary phase matrix, and vert-

ical variation of scattering albedo. Thus, there are fewer a priori restrictive assumptions, such as the required separability of the phase matrix or vertical homogeneity (e.g., Chandrasekhar, 1960; Sekera, 1963, 1966).

Recognizing the potential power of this basic approach, Dave (1970a,b) has developed an approximate analytical formalism for the Mie phase matrix, aimed at decreasing computing time with comparatively little sacrifice in solution accuracy.

The local transfer equation in the form

$$\mu \frac{d\mathbb{I}_v(\tau_v; \mu, \phi)}{d\tau_v} = \mathbb{I}_v(\tau_v; \mu, \phi) - w(\tau_v) \left\{ \frac{1}{4\pi} P(\mu, \phi; -\mu_0, \phi_0) \cdot F e^{-\tau_v/\mu_0} + \frac{1}{4\pi} \int_{-\pi}^{\pi} \int_{-\pi}^{\pi} P(\mu, \phi; \mu', \phi') \cdot \mathbb{I}_v(\tau_v; \mu', \phi') d\mu' d\phi' \right\} - [1 - w(\tau_v)] \mathbb{B}_v(\tau_v) \quad (30)$$

may be formally integrated with respect to optical depth, yielding a non-homogeneous matrix Fredholm integral equation for the Stokes parameters representing the spectral specific intensity. We shall, in what follows, suppress the true emission term in the matrix source function. Inclusion of this term creates virtually no additional difficulties for the solution algorithm, the Planck function simply representing an additional term in the non-homogeneous portion of the integral equation. By the same token, we may assume that the single scattering albedo is unity, without any loss of generality. In this case, the equations governing the p^{th}

Stokes parameter of the upward and downward intensities at the level τ are

$$I_p(\tau_v; \mu, \phi) = \int_{\tau}^{\tau_v} \int_{\omega'} P_{pq}(\Theta) I_q(t; \mu', \phi') d\omega' e^{(I_v - t)/\mu} dt, \bar{\mu}' \\ + \int_{\tau}^{\tau_v} P_{pq} F_q(t; \mu_0, \phi_0) e^{(I_v - t)/\mu} \bar{\mu}' dt \quad (0 \leq \mu \leq 1) \quad (32)$$

$$I_p(\tau; \mu, \phi) = \int_{\tau}^0 \int_{\omega'} P_{pq}(\Theta) I_q(t; \mu', \phi') d\omega' e^{(I_v - t)/\mu} dt, \bar{\mu}' \\ + \int_{\tau}^0 P_{pq} F_q(t; \mu_0, \phi_0) e^{(I_v - t)/\mu} \bar{\mu}' dt \quad (0 \leq \mu \leq 1) \quad (33)$$

In deriving the preceding relations, it has been assumed that the upward intensity at $\tau=\tau_v$ and the downward intensity at $\tau=0$ are each identically zero. (Again, it should be apparent that there is no loss of generality). Thus, half of the intensities at $\tau=\tau_v$ and $\tau=0$ are known, and half are unknown.

Relations (32) and (33) constitute a system of simultaneous equations for the Stokes parameters representing the intensity at the level τ . Herman and Browning's approach to the system can be described as follows. First, it is assumed that the dependent variables are known at some level τ_n . Then, the intensity at some distance from the level τ_n is

given by (we restrict ourselves temporarily to the upward intensity):

$$I_p^{(n+1)}(\mu, \phi) \approx \bar{J}_p(\mu, \phi) \int_{\tau_n}^{\tau_n + \Delta\tau} e^{(\tau_n + \Delta\tau - t)/\mu} dt \\ + I_p^{(n)}(\mu, \phi) e^{-\Delta\tau/\mu} \quad (34)$$

where $\bar{J}_p(\mu, \phi)$ is the value of the p th Stokes parameter of the source function, averaged over the increment $\Delta\tau$.

Writing the source function explicitly, and performing the integration indicated in (34), we obtain

$$I_p^{(n+1)}(\mu, \phi) = I_p^{(n)}(\mu, \phi) e^{-\Delta\tau/\mu} + (1 - e^{-\Delta\tau/\mu}) \int_0^{2\pi} \int_0^\pi P_{pq} \bar{I}_q \sin\theta' d\theta' d\phi' \\ + P_{pq}(\mu, \phi; \mu_o, \phi_o) \bar{F}_q(\mu_o, \phi_o) [1 - e^{-\Delta\tau/\mu}] \quad (35)$$

where \bar{I}_q and \bar{F}_q are the mean values of I_q and F_q over the interval $\Delta\tau$. These averages are taken to be equal to the quantities evaluated at the midpoint of the layer.

Finally, the angular integrations are approximated by sums over a discrete set of angular increments, and average values extracted. Performing all of these operations, and then solving for the intensity at the $(n+1)$ st level, we get (Herman and Browning, 1965, eq. 2.12):

$$I_p^{(n+1)}(\mu, \phi) = I_p^{(n)}(\mu, \phi) e^{-2\Delta\tau/\mu} + P_{pq}(\mu, \phi; \mu_o, \phi_o) F_q^{(n)}(\mu_o, \phi_o) (1 - e^{-2\Delta\tau/\mu}) \\ + (1 - e^{-2\Delta\tau/\mu}) \sum_{\Delta\mu_i} \sum_{\Delta\phi_k} \langle P_{pq}(\mu, \phi; \Delta\mu_i, \Delta\phi_k) I_q^{(n)}(\Delta\mu_i, \Delta\phi_k; (\mu_i - \mu_{i-1})) \rangle \Delta\phi_k \quad (36)$$

The numerical procedure is initiated by writing the preceding relation, for the first level below the "top" of the model atmosphere. To evaluate the summation term, values of $I_p^{(0)}$ for zenith angles corresponding to upward intensity are required. Since these are unknown, they are estimated for this first iteration to be zero. We may now use (36) to estimate $I_p^{(n)}(\mu, \phi)$ for all p and n, down to the lower boundary, thus yielding the first iterate for the upward intensities.

Now, a relation analogous to (36) may easily be derived for the downward intensities. The first iterates for these quantities are obtained by beginning at the lower boundary. However, this time, an estimate for the intensities required for the summation term is available from the first iteration for the upward intensities. In this manner, we obtain the first iterate for the downward intensities. The procedure from this point on is evident. The new estimates of upward intensities are used in (36), thus generating the second iterate for upward intensity. The iteration is continued until successive values of intensity at each level agree to some preassigned tolerance.

5.4 Solution of the Thermal Energetics Problem.

For discussion purposes, the following pair of equations

may be taken as those governing thermal energy exchange in a dust-laden gaseous system (neglecting phase changes):

$$(\underline{s} \cdot \nabla) \mathbb{I}_v(r, s, t) = \frac{\rho k_v^s}{4\pi} \int_{\omega} \underline{P}(\underline{s}, \underline{s}') \mathbb{I}_v(r, \underline{s}', t) d\omega' + K_v^a \rho \mathbb{B}_v[T(r, t)] - \rho (K_v^a + K_v^s) \mathbb{I}_v(r, s, t) \quad (37)$$

$$\rho c_p \frac{\partial T(r, t)}{\partial t} = -\nabla \cdot [K(r, \sigma^*, t) \nabla T(r, t)] + \int_0^\infty K_v^a \left\{ \left[\int_{\omega} \mathbb{I}_v(r, s, t) d\omega' - 4\pi \mathbb{B}_v[T(r, t)] \right] \right\} dv \quad (38)$$

The first relation represents the non-LTE radiative transfer equation (see Sect. 5.2), and the second relates the local time rate-of-change of temperature to the divergence of the total heat flux. $K(r, \sigma^*, t)$ is a generalized heat diffusion coefficient which would include molecular-conductive and/or moderate turbulent heat exchange mechanisms as a function of position r and the static stability σ^* . The symbol $\llbracket \cdot \rrbracket$ designates the sum of the first 2 Stokes matrix components. The unit vector s indicates the direction in which the radiation field is considered.

It should be noted here that it is the radiative net flux divergence which determines the radiative portion of heating. The second term on the right-hand side of eq. (38) represents a transformed expression for the radiative net flux divergence

as presented by, e.g., Bergstrom (1971) and Kondratyev (1969).

For notational convenience, the relations (37) and (38) may be cast into the form

$$\mathcal{L}[\mathbb{I}_v(r, \xi, t)] = [\mathcal{B}_v[T(r, t)]] \quad (39)$$

and

$$\mathcal{L}[T(r, t)] = H[\mathbb{I}_v(r, \xi, t)] + G[T(r, t)] \quad (40)$$

where \mathcal{L} () is a linear integrodifferential operator, \mathcal{P} () is a linear parabolic operator, and H (), and G () are linear and nonlinear integral operators, respectively, whose explicit form may be inferred from relations (37) and (38).

Among the computational algorithms applicable to the nonlinear functional relations (39) and (40) are finite differences schemes (Ames, 1970), nonlinear optimization techniques (Beltrami, 1970), numerical integral transform methods (Bellman, 1969), and linearization approaches (Viskanta and Grosh, 1962; Lick, 1964). It appears, however, that the most promising approach will be through the use of the Newton-

Raphson-Kantorovic (N-R-K) iteration (Lee, 1968).

The N-R-K-iteration is a function-analytic generalization of the Newton root-finding scheme for nonlinear scalar equations. It replaces the nonlinear functional equation with a sequence of linear relations whose solution converges to the solution of the original problem, under certain restrictions on the functional operators and initial iterate. The iteration scheme for relations (39) and (40) would in this context take the form

$$P[\mathbb{I}_v^{(n+1)}] = \left[B_v[T^{(n)}] \right] + \left[T^{(n+1)} - T^{(n)} \right] \left[B_v^f[T^{(n)}] \right] \quad (41)$$

and

$$\begin{aligned} \tilde{\lambda}[T^{(n+1)}] &= H[\mathbb{I}_v^{(n)}] + G[T^{(n)}] \\ &\quad + \left[T^{(n+1)} - T^{(n)} \right] G^f[T^{(n)}] \quad (n=1,2,3,\dots) \end{aligned} \quad (42)$$

where $(\)^f$ represents Frechet-differentiation (Rall, 1969). The eqs. (41) and (42) constitute a linear system for determination of the $(n+1)$ st iterates of temperature and radiative intensity, which may be solved by the methods employed by Lee (1968).

The Newton-Raphson-Kantorovic method generally exhibits quadratic convergence behavior, resulting in a more limited number of iterations required for a given accuracy, as compared with other methods, e.g., contraction mapping. This advantage is particularly attractive when large gradients of the solution vector may be expected near the boundaries of the simulated system (Bellman and Kalaba, 1965). Such is the case for temperature near the surface or at the top of dust layers.

5.5 Modeling of the Time-dependent Thermal Convection Layer Induced by Radiative Surface Heating.

While the scale analysis of Gierasch and Goody (1968) and calculations of relaxation times for the Martian troposphere (Goody and Belton, 1967) indicate that advection of temperature by the planetary-scale wind field is of less importance in determining the vertical temperature profile than the effects of radiative transfer, it does not follow that the effects of small-scale convective heat transport are negligible. The radiative equilibrium calculations of Prabhakara and Hogan (1965), and time-dependent studies by Gierasch and Goody (1968) and Pallmann and Dannevik (1972) indicate that statically-unstable thermal stratification is induced in the lower scale height by the intense surface radiative heating in regions away from the polar cap. Such instability would lead to development of a free-convection layer whose depth would vary over the daylight hours. In addition, it is possible that a detached convection layer would develop at the top of an optically-thick dust layer as a result of efficient radiative heating within the dust layer combined with a sharp variation of emissive power across the top of the layer.

An important feature of such thermal convection layers is that they are capped above and/or below by regions which

are stably stratified, and thus depend upon penetrative mechanisms (convective heat flux opposite the mean temperature gradient) for their growth and maintenance. It is difficult to model this phenomenon with an Austauch parameterization of convective heat flux, because the latter requires a negative eddy conductivity to describe penetrative convection (Kuo, 1968). Furthermore, the application of similarity theory usually requires an assumption relating to existence of a constant flux layer.

An alternative approach to numerical modeling of the time-dependent free-convection layer is to calculate explicitly the convective heat flux by determining the dynamical motion and temperature fluctuation fields. This requires solution of the equations of motion, similar in some respects to that undertaken in the nonlinear Rayleigh-Benard problem. However, for insolation to provide a natural drive for the convection layer, a thermal lower boundary condition is required which is considerably more general than that which is conventionally applied to the classical Benard problem. The required thermal boundary condition is, in fact, the same which has been applied to the radiative-conductive model described in this report.

If the maximum depth of the surface-based free-convection layer is small compared with the scale height of the isen-

tropic atmosphere and we are willing to exclude acoustic waves from the analysis, the appropriate equations for the required numerical model are the Boussinesq approximations to the Navier-Stokes, energy, and continuity equations. Herring (1963, 1964) has developed a spectral model based on these relations, employing the "mean-field approximation." In this formulation, it is assumed that the nonlinear interactions among fluctuations of temperature and velocity are of lesser importance in determining the vertical convective heat transport than the interactions between vertical velocity fluctuations and the mean (horizontally-averaged) vertical temperature profile. Thus, the model is capable of simulating the important mechanism of penetrative convection, but is considerably simpler to handle numerically than the system including the fluctuating interactions.

Musman (1968) has shown that Herring's model is capable of reproducing in some detail the circulation induced by a steady penetrative convection and it also appears (Elder, 1969) that the model is quite successful in the time-dependent case.

In the mean-field Boussinesq approximation, the system of governing equations is closed without the necessity of computing the horizontal velocity components and the deviation of pressure from hydrostatic equilibrium. Thus,

there are three equations for determination of the vertical velocity fluctuations, horizontally-averaged vertical temperature profile, and the fluctuation of the temperature field from the latter profile. In the spectral version of this model, the boundary conditions are automatically satisfied because of the special nature of the basis functions used in the series expansion.

Herring's model can be extended and modified to be compatible with the radiative-conductive model outlined in this report. The required generalized thermal boundary condition would still be applied to the subsoil domain, to determine the new surface temperature at the end of a time-step. This temperature would then furnish the lower boundary condition for the spectral convection model, which would include the effects of radiative transfer. This model would then generate a new atmospheric temperature profile, based on radiative, conductive and convective heat transport. The new profile would furnish the downwardly-directed radiative fluxes required for calculation of a new soil surface temperature and the cycle would be repeated. In this manner, the time-history of the subsoil and atmospheric temperature profiles can be computed, including the combined effects of radiative, molecular-conductive, and thermal-convective heat transport mechanisms.

6.0 Summary of Research and Major Findings

As described in Sections 1 and 2, the wealth of information provided by the Mariner spacecraft series has generated an adequate basis to allow inferences into the primary physical mechanisms likely to be active in Martian atmospheric processes. The high concentration of radiatively-active constituent and the relative tenuity of the Martian atmosphere result in an intense radiative response capability, such that tropospheric heat exchange at scales greater than 10 m is dominated by radiative transfer. By contrast, terrestrial radiative relaxation of thermal perturbations is at least 30 times slower, i.e., \sim 10 days for large-scale motion. In addition, the global extent of sand-like dry soil material permits insolation to induce a large diurnal soil surface temperature variation in the regions away from the polar ice cap. Over the dry ice, the surface temperature is fixed at the CO_2 sublimation point, regardless of the variation of insolation. Because of its radiative responsiveness, the lowest several km of the Martian atmosphere directly responds, in either case, to the thermal conditions at the lower boundary. The resulting large thermal gradients near the ground-atmosphere interface

make molecular thermal conduction an important mechanism in coupling the sub-surface and atmospheric thermal structure. When atmospheric strata are dust-laden, an additional radiation table is provided at the top of the dust layer, which acts radiatively like a "secondary surface," significantly influencing atmospheric thermal structure in the layers above and below. Thus, secondary thermal boundary layers are induced.

The physical mechanisms having primary roles in the determination of thermal structure in the Martian ground-atmosphere system are such that a numerical model of the time-dependent structure of thermal boundary layers can be constructed without the need to consider directly the atmospheric motion field. This model has been described in Sections 2 and 3. Some of the more important results derived through basic numerical experiments with the model are as follows:

- (1) when there is little dust present in the Martian atmosphere, and in regions away from the polar ice caps, weak-and strong-line radiative communication produces three primary atmospheric regimes. The lowest, characteristically of 3 km depth, responds directly through strong-line

radiative transfer and molecular thermal conduction to surface temperature variation. The middle regime, extending to \sim 30 km altitude, is in weak-line communication with surface temperature variation, but also undergoes direct solar heating and losses to outer space. The upper regime is dominated by the upper boundary conditions, i.e., solar heating and emissive losses, and is affected little by conditions at the surface.

- (2) the presence of an atmospheric dust layer which is optically-thick in the near-IR ranges induces secondary thermal boundary layers at the extremities of the layer, because of the sharp variation of radiative properties. For example, diurnal temperature variation at the top of a dust layer of 30 km thickness may be as much as 50% of the soil-surface temperature variation.
- (3) midlatitudinal temperature soundings derived by inversion of Mariner 9 IRIS measurements obtained during the dust-laden period of the mission, undergo considerable modification when used as initial data in the simulation model. There is some indication that the IRIS-derived profiles, obtained

from an inversion technique assuming a dust-free atmosphere, represent a highly smoothed version of the actual thermal structure of the dust-laden layers.

- (4) in the polar region, the temperature of the dry ice surface is rigidly maintained at 148K, the sublimation temperature of CO₂ at a Martian surface pressure of 6 mb. The heat transfer mechanisms at such an interface are dominated by this constraint. The simulative outputs indicate that the planetary atmospheric counter-radiation plays an important role in the heat flux balance at the interface. The persistency of the heat sink at the dry ice surface removes rather large amounts of heat from the atmosphere by conductive and radiative processes. In contrast, polar ice-free sand surfaces are not only warmer and maintain variable temperatures but also permit the tropospheric layers to respond to surface heating/cooling.
- (5) the time-dependent simulated temperature structure in the atmosphere over a frost-free surface of the polar region is found to vary between 220K and 235K. These results are rather closely represented by the Mariner 9 IRIS sounding. However, if the

underlying surface is frost-covered the simulated temperature profiles are substantially cooler.

The outputs from our model indicate that a large fraction of the frost-surface emission does not penetrate the dust layer.

In Section 5, the theoretical framework of a refined version of the simulation model has been presented. Experience with the current version of the model shows that among the areas requiring refinement are (1) the treatment of the impact of non-conservative multiple Mie-scattering by particulates on thermal energetics transfer, and (2) the incorporation of free-convective heat transport mechanisms to accomodate the impact of statically-unstable temperature distributions induced by radiative exchange.

It is shown that the impact of multiple Mie scattering on thermal energetics can be incorporated by solving simultaneously the heating-rate equation and the radiative transfer equation including the scattering terms. A local iterative scheme based on the Newton-Raphson-Kantorovic and Gauss-Seidel algorithms is suitable for the resulting system of equations.

In addition, a method for incorporating free-convective heat transfer into the simulation model has been outlined. This scheme is based on a spectral version of the equations applicable to the Rayleigh-Benard problem, with a generalized lower boundary condition to allow thermal coupling between the ground and atmospheric subsystems, and to permit insolation to provide a natural driving mechanism. It is shown that this approach is compatible with the radiative-conductive model including the effects of particulate multiple scattering and absorption.

REFERENCES

- Adams, C. and G. Kattawar, 1970: Solutions of the equations of radiative transfer by an invariant imbedding approach. J. Quant. Spec. and Rad. Trans., 10, 341-356.
- Ames, W., 1970: Numerical Solutions of Partial Differential Equations. New York, Academic Press, 291 pp.
- Bellman, R. E., 1969: Numerical Inversion of Laplace Transforms. New York, American Elsevier Co., 249 pp.
- _____, and R. E. Kalaba, 1965: Quasilinearization and Nonlinear Boundary Value Problems. New York, American Elsevier Co., 206 pp.
- Beltrami, E. J., 1970: An Algorithmic Approach to Non-linear Analysis and Optimization. New York, Academic Press, 235 pp.
- Bergstrom, R. W., 1971: The effects of urban air pollution on solar heating and turbidity. Preprints from Conference on Air Pollution Meteorology. Presented at Rayleigh, North Carolina, 93-97.
- Busbridge, I., 1960: The Mathematics of Radiative Transfer. London, Cambridge University Press, 143 pp.
- Chandrasekhar, S., 1960: Radiative Transfer. New York, Dover Publ., 393 pp.
- Collatz, L., 1969: Functional Analysis and Numerical Mathematics. New York, Academic Press, 473 pp.
- Dave, J., 1964: Meaning of successive iteration of the auxiliary equation of radiative transfer. Astr. J., 140, 1292-1303.
- _____, 1965: Multi-scattering in a non-homogeneous atmosphere. J. Atmos. Sci., 22, 273-279.
- _____, 1969: Effect of coarseness of integration increment on the calculation of the radiation scattered by polydispersed aerosols. Appl. Opt., 8, 1161.

- _____, and J. Gazdag, 1970a: A modified fourier transform method for multiple scatterings in a plane-parallel mie atmosphere. Appl. Opt., 9, 1457-1466.
- Diermendjian, D., 1969: Electromagnetic scattering on spherical polydispersions. Rand Rept. R-456-PK, Santa Monica, California, 290 pp.
- Elder, J., 1969: The temporal development of a model of high Rayleigh number convection. J. Fl. Mech., 35, 417-437.
- Elsasser, W. M., 1960: Atmospheric radiation tables. Amer. Meteor. Soc., monograph 23, Boston, American Meteorological Society.
- Gierasch, P., 1971: Dissipation in atmospheres: the thermal structure of the Martian lower atmosphere with and without viscous dissipation. J. Atmos. Sci., 28, 315-324.
- _____, and R. M. Goody, 1968: Studies of the thermal and dynamical structure of the Martian lower atmosphere. Planetary Space Sci., 16, 615-646.
- _____, and _____, 1972: The effect of dust on the temperature of the Martian atmosphere. J. Atmos. Sci., 29, 400-402.
- Goody, R. M., 1964: Atmospheric Radiation. London, Oxford Clarendon Press, 436 pp.
- _____, and M. Belton, 1967: Radiative relaxation times for Mars; a discussion of Martian atmospheric dynamics. Planetary Space Sci., 15, 247-256.
- Hansen, J., 1969: Radiative transfer by doubling very thin layers. Astro. J., 155, 565-573.
- _____, 1971: Multiple scattering of polarized light in planetary atmospheres. J. Atmos. Sci., 28, 120-125.
- Herman, B. M. and S. Browning, 1965: A numerical solution of the equation of transfer. J. Atmos. Sci., 22, 559-566.
- Herring, J., 1963: Investigations of problems in thermal convection. J. Atmos. Sci., 20, 325-338.

_____, 1964: Investigation of problems in thermal convection: rigid boundaries. J. Atmos. Sci., 21, 227-290.

Irvine, W., 1968: Multiple scattering by small particles. Astro. J., 152, 823-834.

Jet Propulsion Laboratory, 1968: Mars scientific model. Vol. 1. JPL Document No. 606-1.

Kondratyev, K. Ya., 1969: Radiation in the Atmosphere. New York, Academic Press, 912 pp.

Kuo, H. L., 1968: The thermal interaction between the atmosphere and the earth and propagation of diurnal temperature waves. J. Atmos. Sci., 25, 682-706.

Lee, E. S., 1968: Quasilinearization and Invariant Imbedding. New York, Academic Press, 329 pp.

Lick, W., 1964: Transient energy transfer by radiation and conduction. International J. Heat Mass Trans., 8, 119-127.

Mussman, S., 1968: Penetrative convection. J. Fluid Mech., 31, 343-360.

Pallmann, A. J., 1968: Radiative heating and cooling functions for the lower Martian atmosphere under the condition of local thermodynamic equilibrium. NASA CR-1044, 40 pp.

_____, and W. P. Dannevik, 1972: Transient variation of Martian ground-atmosphere thermal boundary layer structure, Preprints from Conference on Atmospheric Radiation. Boston, American Meteorological Society.

_____, and S. P. Frisella, 1972: Numerical simulation of radiative-conductive heat transfer in the Martian atmosphere-polar cap utilizing mariner 9 IRIS data. Preprints from Conference on Atmospheric Radiation. Boston, American Meteorological Society.

- Prabhakara, C. and J. S. Hogan, 1965: Ozone and carbon dioxide heating in the Martian atmosphere. J. Atmos. Sci., 22, 97-109.
- Preisendorfer, R. W., 1965: Radiative Transfer on Discrete Spaces. New York, Pergamon Press, 459 pp.
- Rall, L. B., 1969: Computational Solutions of Nonlinear Operator Equations. New York, Wiley, 224 pp.
- Richtmyer, R. D. and K. W. Morton, 1967: Difference Methods for Initial Value Problems. New York, Interscience, Wiley, 405 pp.
- Saaty, T. L., 1967: Modern Nonlinear Equations. New York, McGraw-Hill, 473 pp.
- Samuelson, R., 1965: Radiative transfer in a cloudy atmosphere. NASA TR-R215.
- Sekera, Z., 1963: Radiative transfer in a planetary atmosphere with imperfect scattering. RAND Report R-413-PR, Santa Monica, California.
- , 1966: Reduction of the equations of radiative transfer for a plane-parallel planetary atmosphere, part I. RAND Memorandum RM-4951-PR, Santa Monica, California.
- Sellers, P., 1965: Physical Climatology. University of Chicago Press, 272 pp.
- Shahrokhi, F. and P. Wolf, 1968: Radiation heat transfer in absorbing, scattering, and emitting medium. NASA CR-1023.
- Sparrow, E. M. and R. D. Cess, 1966: Radiation Heat Transfer. Belmont, California, Brooks/Cole Publ. Co., 322 pp.
- Stull, V. R., P. J. Wyatt and G. N. Plass, 1963: The infrared absorption of carbon dioxide. Infrared Transmission Studies III. Rpt. Contract SSD-TDR-62-127, Space Systems Division, Air Force Systems Command, Los Angeles, California,

Viskanta, R. and R. J. Grosh, 1962: Heat transfer by simultaneous conduction and radiation in an absorbing medium, J. Heat Trans., 63-72.

Zdunkowski, W. G. and D. C. Trask, 1971: Application of a radiative-conductive model to the simulation of nocturnal temperature changes over different soil types. J. Appl. Met., 10, 937-948.

NATIONAL AERONAUTICS AND SPACE ADMINISTRATION
WASHINGTON, D.C. 20546

OFFICIAL BUSINESS
PENALTY FOR PRIVATE USE \$300

SPECIAL FOURTH-CLASS RATE
BOOK

POSTAGE AND FEES PAID
NATIONAL AERONAUTICS AND
SPACE ADMINISTRATION
45¢



POSTMASTER : If Undeliverable (Section 158
Postal Manual) Do Not Return

"The aeronautical and space activities of the United States shall be conducted so as to contribute . . . to the expansion of human knowledge of phenomena in the atmosphere and space. The Administration shall provide for the widest practicable and appropriate dissemination of information concerning its activities and the results thereof."

—NATIONAL AERONAUTICS AND SPACE ACT OF 1958

NASA SCIENTIFIC AND TECHNICAL PUBLICATIONS

TECHNICAL REPORTS: Scientific and technical information considered important, complete, and a lasting contribution to existing knowledge.

TECHNICAL NOTES: Information less broad in scope but nevertheless of importance as a contribution to existing knowledge.

TECHNICAL MEMORANDUMS: Information receiving limited distribution because of preliminary data, security classification, or other reasons. Also includes conference proceedings with either limited or unlimited distribution.

CONTRACTOR REPORTS: Scientific and technical information generated under a NASA contract or grant and considered an important contribution to existing knowledge.

TECHNICAL TRANSLATIONS: Information published in a foreign language considered to merit NASA distribution in English.

SPECIAL PUBLICATIONS: Information derived from or of value to NASA activities. Publications include final reports of major projects, monographs, data compilations, handbooks, sourcebooks, and special bibliographies.

TECHNOLOGY UTILIZATION PUBLICATIONS: Information on technology used by NASA that may be of particular interest in commercial and other non-aerospace applications. Publications include Tech Briefs, Technology Utilization Reports and Technology Surveys.

Details on the availability of these publications may be obtained from:

SCIENTIFIC AND TECHNICAL INFORMATION OFFICE

NATIONAL AERONAUTICS AND SPACE ADMINISTRATION

Washington, D.C. 20546